The effect of molecular fluctuations on hole diffusion within dye monolayers

Valérie Vaissier,[*,†] Edoardo Mosconi,[‡] Davide Moia,[†] Mariachiara Pastore,[‡] Jarvist M. Frost,[¶] Filippo De Angelis,[*,‡] Piers R. F. Barnes,[†] and Jenny Nelson[*,†]

Imperial College London, Computational Laboratory for Hybrid/Organics Photovoltaics, CNR-ISTM, Via Elce di Sotto 8, 06123, Perugia, Italy, and University of Bath

E-mail: valerie.vaissier10@imperial.ac.uk; filippo@thch.unipg.it; jenny.nelson@imperial.ac.uk

Abstract

Measured hole diffusion coefficients in dye monolayers are larger than can be explained by a charge hopping model with a static distribution of parameters describing intermolecular hole transfer. We show that large amplitude fluctuations of the tethered dye configurations on the surface could explain the observed diffusion rates by enabling charges trapped in particular configurations to escape as the dye orientations change. We present a multiscale model of hole transport which includes the effect of dynamic rearrangement of the monolayer of anchored dyes. Conformations of pairs of indolene dye molecules (both D102 and D149) were generated by a rigid molecular packing algorithm and Car-Parrinello molecular dynamics to mimic the conformational and configurational disorder of a dye monolayer adsorbed to an anatase (101) titanium dioxide surface. The electronic coupling (J_{ij}) for each pair of neighbouring dyes was calculated to build distributions representing the disorder in a real system. These

[*]To whom correspondence should be addressed

[†]Imperial College London

[‡]Computational Laboratory for Hybrid/Organics Photovoltaics, CNR-ISTM, Via Elce di Sotto 8, 06123, Perugia, Italy

[¶]University of Bath

values were used as inputs to Marcus' non adiabatic equation for charge transfer to calculate the rate of hole hopping for each pair. Hole diffusion was simulated with a continuous time random walk, accounting for different timescales of molecular rearrangement (changes in the dye geometry). The dynamic nature of configurational disorder was captured by reassigning the values of J_{ij}, drawn from the aforementioned distributions, after a fixed renewal time. We found hole diffusion coefficients of 3.3×10^{-8} and 9.2×10^{-8} cm^2s^{-1} for D102 and D149 respectively for a renewal time of 10^{-7} s. This is in good agreement with the corresponding measured coefficients for D102 and D149 of 9.6×10^{-8} and 2.5×10^{-7} cm^2s^{-1} whilst the diffusion coefficients are underestimated by at least a factor of 15 if the dynamics are ignored. Fast rearrangement of dye monolayer configuration may explain the high lateral hole diffusion coefficients explained experimentally. Our results indicate that both chemical structure and the availability of different packing configurations must be considered when designing conductive molecular monolayers.

Keywords : charge transfer, dye molecule, lateral hole hopping, electronic coupling, configurational disorder, diffusion, continuous time random walk

Dye sensitised semiconductors have sparked wide interest in many energy-related fields, most particularly photovoltaics and solar fuel production. They consist of a compact or mesoporous metal oxide film at the surface of which is adsorbed a monolayer of dye molecules. In the Dye Sensitised Solar Cell (DSSC),[1,2] the absorption of photons takes place within the dye molecule monolayer. Exciton splitting occurs when the electron is injected into the subjacent metal oxide film (often TiO_2) while the hole remains on the dye molecule. In the conventional model of DSSC operation, the dye is then directly reduced to its neutral state by the surrounding Hole Transporting Medium (HTM). However, it has been observed in several instances that the hole can diffuse laterally between dyes in monolayer, across the surface of the metal oxide.[3–5] This alternative charge pathway could serve as a transport mechanism for holes in the solid state DSSCs, where poor physical contact between the dye monolayer and the HTM is hypothesised to be a bottleneck for photocurrent generation.[6] This phenomenon of lateral hole hopping can also be considered in the context of the transport of charges to catalytic sites for water splitting or solar fuel production,

molecular transistors, batteries or any other molecular electronic device.[7–15] Therefore, being able to predict the kinetics of charge diffusion within a molecular monolayer is of significant interest. Identifying the key factors enhancing charge diffusion in this context will lead to the derivation of design rules for efficient hole conductive molecular wires.

In this paper, we focus on lateral hole transport between dyes on sensitised TiO_2 nanocrystalline films such as those used in DSSCs and solar fuel photo electrodes. Specifically we develop a computational framework over a range of length and time scales enabling the relationship between molecular configuration and the bulk diffusion coefficient of holes to be established. Experimentally, hole diffusion has been observed to depend on the nature of the dye and surrounding medium. This is rationalised given that the chemical structure of the dyes and their physical arrangement in a given system will control their electronic interactions and hence the conductivity of the monolayer. Nevertheless, a clear link between the variables governing charge transfer (at the nanoscale) and the measured observables (diffusion coefficients at the microscale) is still missing.[16,17] We need to understand the relationship between these scales to develop design rules for developing conductive molecular monolayers.

Intuitively we expect the lateral hole hopping rate to depend on the separation between dye molecules which, in turn, depends on the density (or loading) of molecules on a given surface and the electronic coupling between charge donor and acceptor, (which is strongly dependent on the geometry of the pair of molecules) and on the dynamics of molecular rearrangement. Experimentally, such information is accessible only on average, for a macroscopic film, while for a microscopic model one needs the structure of the monolayer at the nanoscale over the time interval on which charge transfer occurs. Therefore, we need to know not only the chemical structure and attachment points of the dyes on the semiconductor surface but also the dynamics of conformational changes and the range of configurations explored by the anchored dye molecules.[18] Here we combine quantum chemical calculations of electronic structure and coupling with ab-initio Molecular Dynamics within the Car-Parrinello framework (CPMD)[19] or rigid molecular packing (RMP) and kinetic Monte Carlo[20,21] in order to include the conformational dynamic changes within the

transport simulation.

Previously, simulations of charges percolating through a dye monolayer have been published to rationalise lateral hole hopping in DSSC.[3,8] However, no study has yet attempted to combine hole transport with dye dynamics. The influence of the dynamical disorder on charge transfer rates have been extensively studied for biological systems[22–27] but its subsequent effect on macroscopic quantities is missing.

Many multiscale models treating configurational disorder have been published for conjugated polymer systems but either neglect its dynamic nature[28,29] or exclusively take the average of the coupling to calculate charge mobilities.[18,24] Although it has been shown that configurational disorder and in particular the relative orientation of neighbouring charge carriers subunits strongly affects the charge transfer integral hence the mobility,[18,28–30] the effect of the reorientation of these subunits over times similar to charge hopping has not been studied.

Other models for charge transport in organic semiconductors crystals reveal the importance of both static and dynamical disorder to calculate realistic charge mobilities,[16,31] the latter causing the relative localisation of electronic states within the lattice.[32,33]Dynamical disorder also enables the detrapping of charges by allowing the occurrence of more carriers configurations compatible with an hopping event.

Integrating transport with molecular dynamics is a difficult problem. In a fully quantum mechanical picture, the Hamiltonian describing electronic coupling should be continually updated for the new conformations in a self consistent manner.[17] This is most important for systems with a high degree of order, such as organic semiconductors.[17] In our work, to reduce computational cost for our more disordered system, we take an approximate approach and decouple molecular conformation and electronic coupling.

We studied two indolene dye molecules, D102 and D149 (Figure 1), adsorbed on the TiO_2 anatase (101) surface. These dyes have differing degrees of conformational disorder on the surface and possibly a different surface coverage due to different packing motifs. This allows us to examine the influence of this disorder on transport. We have also measured the apparent diffusion coefficient

of holes across a nano crystalline film (D_{exp}).[34] We choose these dyes because they perform well in solid state DSSC[35,36]and their hole diffusion coefficient is amongst the highest reported.[34,37] Also, their anchoring mode and absorption pattern on the (101) TiO_2 surface have already been studied.[38,39] The anatase (101) surface corresponds to a large fraction of the TiO_2 nanoparticles surface[40,41] and we expect the calculated kinetics to approximate the experimental data well.

Our modelling approach overcomes the difficulties of deriving a macroscopically observable quantity for a disordered system based on fundamental calculations of processes occurring on a much shorter timescale. We will show that including the effects of tethered molecular motion enables us to account for unexpectedly high diffusion coefficients.

Results and discussion

This section is organised as follows. First, we describe the degrees of freedom of indolene dyes adsorbed on a anatase surface. From this we explain how we compute sets of pair geometries spanning the range of expected configurational and conformational arrangements. Second, we calculate the electronic coupling distribution obtained for these pair geometries. Finally we present the results of our transport simulations and discuss the influence of dynamic configurational disorder on the hole diffusion coefficient.

Arrangement of D102 and D149 on the (101) TiO_2 surface.

Indolene dye molecules bind to the five-coordinated titanium atoms of the TiO_2 surface by their carboxylate group (see Figure 1a and b), in a bidendate fashion (Figure 1 caption).[42,43] The packing arrangement of D102 and D149 dyes on the anatase surface is given in Figure 1c where (xy) is the plane of the (101) surface. The basis of vectors $\{\mathbf{a}_{\mathrm{D102}}, \mathbf{b}_{\mathrm{D102}}\}$ and $\{\mathbf{a}_{\mathrm{D149}}, \mathbf{b}_{\mathrm{D149}}\}$ generate the lattice of attachment points for D102 and D149 respectively. The norm and directions of these vectors were previously determined by Pastore et al[38] by finding the dimers of lowest energy. We assume full coverage of the TiO_2 surface, this is expected in experimental systems for sufficient

dye exposure.[3,8,44] Furthermore the molecular density of D102 and D149 resulting from the arrangement shown in Figure 1c is consistent with the measured dye loading and coverage for the same system.[34,38,45]

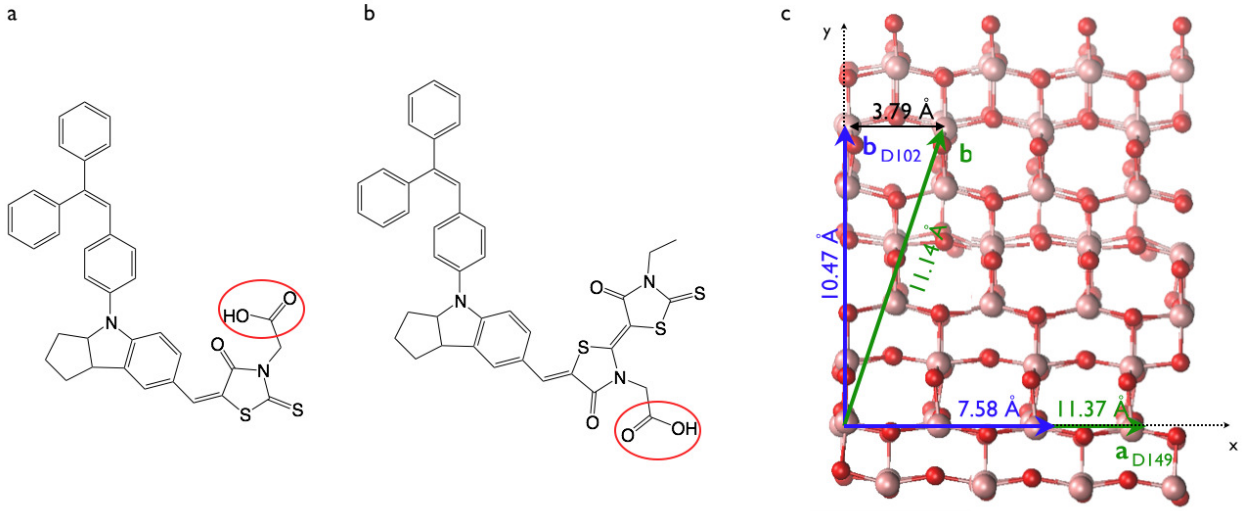

Figure 1: Chemical structure of D102 (a) and D149 (b). The anchoring group to the TiO_2 surface is circled in red in both cases. We assume that the dye molecules bind to the surface in a bidendate mode where the two oxygens of the deprotonated acid carboxylic group are attached to different five coordinated titanium atoms. (c) The most energetically favourable intermolecular spacing for D102 (blue) and D149 (green).[38] The (xy) plane shows the (101) TiO_2 surface.

Since the dyes adopt a bidendate anchoring mode, there are two possibilities for one molecule to sit on the surface (see Figure 2a); this determines the relative orientation of two molecules in a pair. Because D102 and D149 are not symmetric about the anchoring group we expect these different configurations to have a potentially important impact on the electronic coupling.

We refer to the combination of binding modes as the configuration (see Figure 2b to 2d) and the shape of the molecule for a given binding as its conformation.

Furthermore, as seen in Figure 1c, since two neighbouring dyes sit close to each other on the anatase surface we expect intermolecular interactions to influence the set of possible conformations adopted by a pair of dyes on the surface. We address the variety of conformations in two ways. First, in order to sample the conformations explored on short times, less than the time for a typical charge transfer event ($\sim$1ns), we use Car-Parrinello Molecular Dynamics (CPMD , see Methods).

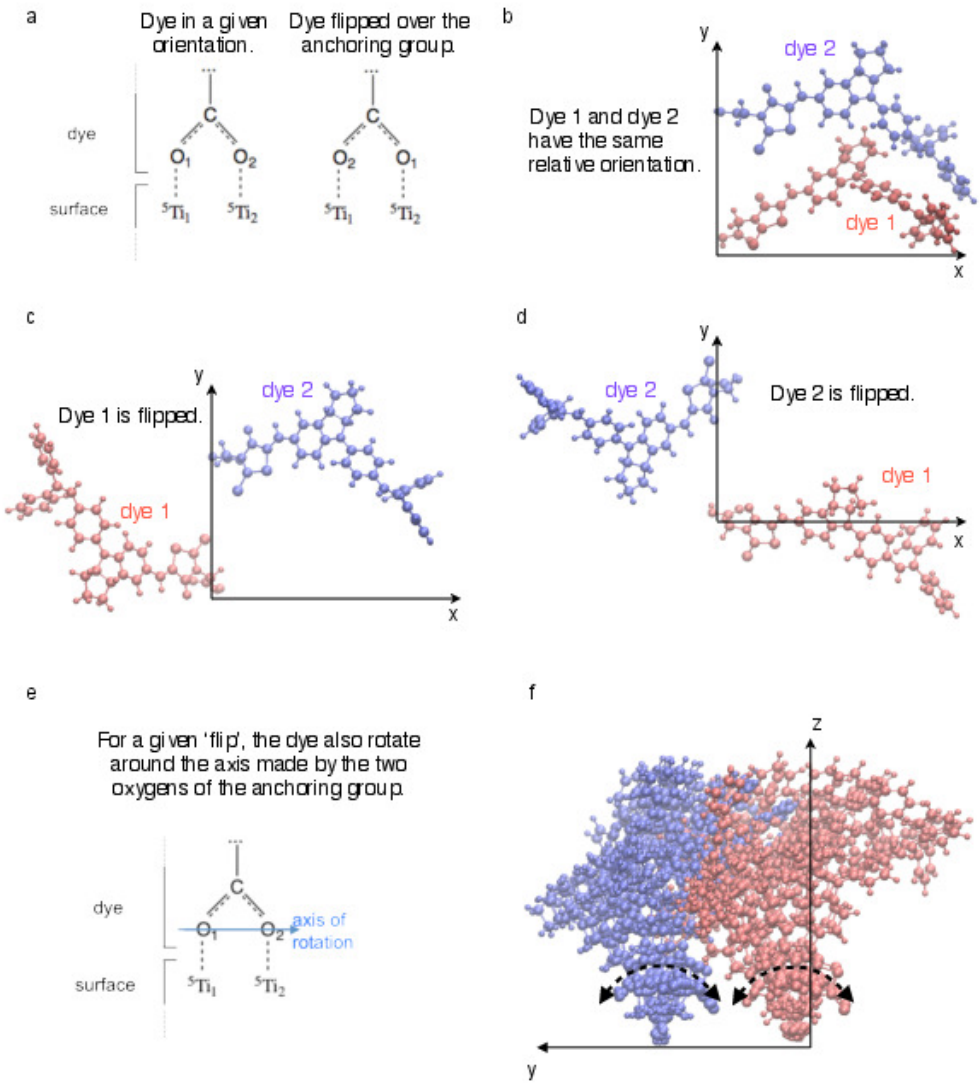

Figure 2: (a) Schematic of the two different orientations one dye molecule can take when attached to the TiO_2 surface. For clarity, only the atoms directly involved in the binding are shown. The subscripts refers to the label of the atom. (b), (c) and (d) Top view of a pair of D102 separated by $\mathbf{b}_{\mathrm{D102}}$ as generated by PACKMOL.[46,47] The two dyes can adopt the same relative orientation (b) or one dye of the pair is flipped around its anchoring foot (c and d). (e) Schematic of the rotational degree of freedom considered in this study. (f) Space spanned by the different conformations of a D102 pair where the two molecules are separated by $\mathbf{b}_{\mathrm{D102}}$; due to the rotational degree of freedom.

The space explored by the different conformations from the CPMD trajectory is visualised in Figure 3 as a superposition of the sampled geometries. However, to explore the conformations visited on time scales longer than charge hopping times we must use a less expensive method since at present the cost of practical CPMD simulations limit them to tens of picoseconds. Here we approximate the set of conformations by those that are compatible with rotations of the dyes around their bidentate binding sites defined by the two oxygens of the anchoring group (see Figure 2e and 2f).

For the longer times, we generate sets of pair geometries obeying the spatial constraints of the anchor points on the surface with a packing optimisation package (PACKMOL, see Rigid Molecular Packing (RMP) in Methods for details). Whilst the CPMD generates a set of conformations obeying thermodynamic equilibrium and allows for molecular fluctuations, the second (rigid rotation) generates a much cruder approximation to the likely conformations which does not allow changes to the molecular shape (see Figure 2f) nor does it generate a means of sampling the conformations that represents thermodynamic equilibrium. Nevertheless this crude approximation allows us to explore the effect of conformational variation on long time scale at relatively low computational cost.

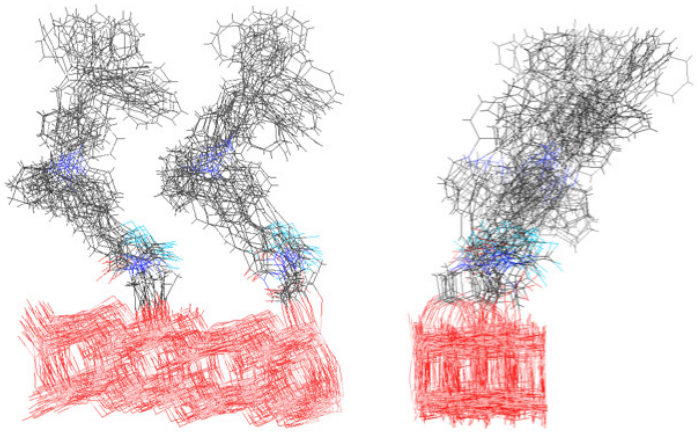

Figure 3: Illustration of the space spanned by the different conformations of a D102 pair where the two molecules are separated by $\mathbf{b}_{\mathrm{D102}}$ (see Figure 1). The two figures are a superimposition of 10 frames, taken at regular interval of a 9 picosecond CPMD trajectory. The left hand side is a view along the x-axis while the right hand side is a view along the y axis.

These two methods both generate a set of conformations for each configuration of dye pairs considered. In the case of the CPMD, the set of conformations conform to thermodynamic equilibrium whilst in the case of the rigid rotation different angles are sampled with equal probability since we have no means to define an equilibrium sample. Consequently the sampling of molecular pairs will be weighted by a Boltzmann distributed sampling of the pair-wise intermolecular potential energy, as calculated with the Universal Force Field (UFF) to simulate pair conformations at thermal equilibrium (see Supporting Information). Then, we calculate the electronic coupling between the Highest Occupied Molecular Orbitals (HOMO) for every molecule pair giving representative distributions of the orbital overlap integral J_{ij} accounting for configurational and conformational disorder within the dye monolayer.

Influence of configurational disorder on electronic coupling

We calculate the electronic coupling, J_{ij} with the projective method[48] (as detailed in Methods) which gives the matrix coupling element between the molecular orbitals involved in the charge transfer event (HOMO here).[49–51] We use the projective method because it is known to improve significantly on the more traditional dimer energy splitting method for intermolecular charge transfer (also see Supporting Information).[52,53]

In D102 and D149, the HOMO as calculated using B3LYP/TZVP-6D is delocalised over the entire molecule (see Supporting Information). Sampled coordinates of molecular pairs from both the CPMD trajectory and the RMP were used as inputs into a molecular pair calculation in vacuum (Gaussian 09 B3LYP/LANL2DZ) with the projective method to calculate distributions of transfer integrals J_{ij}.

Figure 4 shows the density plots of the square electronic coupling calculated for the conformations sampled by CPMD (green curve) in anticipation to its incorporation within Marcus formula of the rate of charge transfer (cf. Equation 4). For completeness we also show the fluctuations of the original J_{ij} data over the simulated time in Supporting Information.

For D102 separated by $\mathbf{a}_{\mathrm{D102}}$ (4a), $\mathbf{b}_{\mathrm{D102}}$ (4b) and D149 separated by $\mathbf{b}_{\mathrm{D149}}$ (4d), we observe

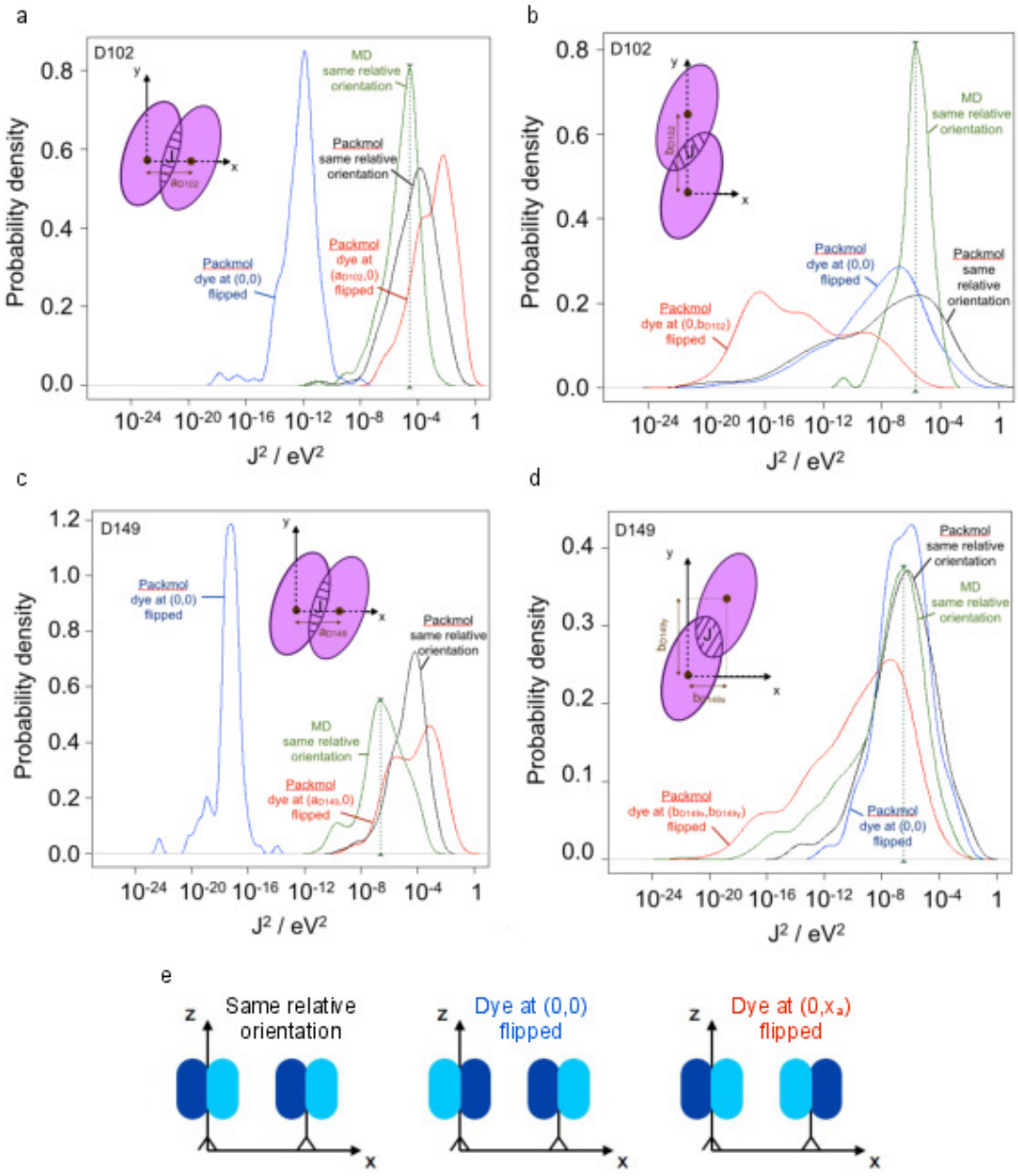

Figure 4: Probability density distributions of the logarithm of the square electronic coupling (in eV^2) for the different pair configurations. The insets illustrate the spacing of the dyes as given in Figure 1c. (a) D102 aligned along the separated by $\mathbf{a}_{D102}$. (b) D102 separated by $\mathbf{b}_{D102}$. (c) D149 separated by $\mathbf{a}_{D149}$ (d) D149 separated by $\mathbf{b}_{D149}$. (e) Schematic of the three configurations considered in this work.

narrow distributions with a peak position around $10^{-6}\mathrm{eV}^2$ (see the dotted green lines in Figures 4a to 4d for guidance). This implies that the fluctuations in pair geometry sampled by the CPMD are rather small. In contrast, for D149 separated by $\mathbf{a}_{\mathrm{D149}}$, the distribution is much wider and slightly shifted towards weaker couplings which is assigned to the effect of steric hindrance pushing the dyes apart.

However, the CPMD calculations do not sample the full set of possible conformations because of limited simulated time (25ps). To study the effect of a wider range of conformations on the electronic coupling we also show J_{ij}^2 distributions from RMP where different angles of rotation of the dye around its anchoring group are sampled uniformly. This is done for the three different configurations, as explained previously and illustrated in Figure 2.

The CPMD has only been performed for pairs of dye having the same relative orientation. Therefore the range of electronic couplings sampled by CPMD can be compared with the distribution due to PACKMOL for the same orientations only (black curve). The peak position of the distributions for the two sampling methods are similar for D102 separated by $\mathbf{b}_{\mathrm{D102}}$ and D149 separated by $\mathbf{b}_{\mathrm{D149}}$ (see Figures 4b and 4d). For D102 separated by $\mathbf{a}_{\mathrm{D102}}$ and D149 separated by $\mathbf{a}_{\mathrm{D149}}$ (Figures 4a and 4c), it appears that the CPMD generates distribution slightly shifted towards weaker couplings. This suggests that in this direction RMP is underestimating the true extent of steric repulsion of the dye molecules, compared to a more full treatment by CPMD.

Comparing Figure 4a (D102 separated by $\mathbf{a}_{\mathrm{D102}}$) and Figure 4c (D149 separated by $\mathbf{a}_{\mathrm{D149}}$) we can see that the ordering of the distributions for particular types of configurations is the same for D102 and D149 for separation by $\mathbf{a}_{\mathrm{D102}}$ and $\mathbf{a}_{\mathrm{D149}}$ respectively. This is consistent with the fact that the pairs are aligned along the same direction on the anatase (101) surface (see Figure 1). Furthermore, we notice a similar peak position for all but one distribution. One possible interpretation of these results is as follows. Even though the attachment points of D149 on the anatase surface are further apart than the ones of D102, the molecule itself is bigger and, overall, the magnitude of the HOMO overlap is similar in both cases. The exception is for the configuration where the dye at the origin of the coordinate axis is flipped with respect to the other one. In this

case, the main part of the dyes are separated by the full length of the lattice vector and this could explain why D149 shows a weaker coupling. In the case where the dye at (a_{D102},0) or (a_{D149},0) is flipped, the main part of the dye is facing outwards; allowing the molecules to overlap significantly compared to when they have the same relative orientation.

In Figure 4d (D149 separated by $\mathbf{b}_{\mathrm{D149}}$) we observe that all distributions have the same peak position ($\sim 10^{-6}\mathrm{eV}^2$) and somewhat similar shape. This implies that the configuration has little influence on the molecular overlap in this configuration. Nevertheless, it appears that more conformations are compatible with the spatial constraints of the neighbouring molecules in two cases, generating tails in the distributions. In contrast, the configuration has strong influence on the electronic coupling for D102 (in Figure 4b). The different configurations for this last case are illustrated in Figure 2. For example Figure 2e corresponds to the red curve in Figure 4b. Because the bigger lobes of the dye face each other, the two molecules tend to lean in opposite directions due to steric hindrance. This relatively large separation between the molecules leads to a wide distribution of weak electronic couplings. When the lobes both face away from the neighbouring dye (Figure 2 f) the molecules lean together leading to a distribution with stronger electronic couplings.

Electronic coupling distributions allow us to calculate the rate of charge transfer for each pair conformation and configuration (see Methods). To simulate hole diffusion at the scale of the film, we incorporate this rate into a kinetic Monte Carlo simulation of hole diffusion.

Influence of the configurational disorder on the kinetics of hole diffusion

In this section we incorporate the electronic coupling distributions in a Continuous Time Random Walk algorithm (CTRW[20,21,54]) to simulate hole diffusion across the dye molecule monolayer (see Methods). The adaptive time step, t_{wait} after which a hole changes site depends on the rate of charge transfer, hence on the square of the electronic coupling, J_{ij}^2, between nearest neighbours. Therefore, we have to consider the relative time scales of the various configurational changes with respect to the hole hopping to properly integrate the J_{ij} distributions within the CTRW algorithm.

The electronic coupling is calculated from the projection of the HOMO of one dye on to that of

its neighbour using the method described in Methods.[48,52,53] For each configuration we estimate the average hopping rates by finding the average $< J_{ij}^2 >$ for all dye conformations (see Supporting information). The resulting average square electronic coupling ranges from 1×10^{-5} to 1×10^{-3} eV^2. Using non adiabatic Marcus theory for the transfer rate (see Methods) and a calculated reorganisation energy in solution of 0.961 and 0.896 eV for D102 and D149 respectively (see Methods), the resulting average hole hopping time varies from 6×10^{-10} to 6×10^{-8} seconds. Regarding the dynamics of dye movements on the surface, we expect fluctuations on a timescale ranging from femtosecond for fast vibrational motions to microsecond for rotations of the whole molecule around its binding sites. The dye hopping times are intermediate between these time scales, therefore we need to find a way to integrate dye and charge dynamics in the same model.

To treat the problem properly we would need a statistical ensemble of conformations that spans the full range of dye dynamics. But since this is too computationally expensive we use the cheaper RMP generated conformations to include the effect of changing conformations on hopping. In this approach, the fastest dynamics are neglected. To examine this approximation we use our CPMD generated ensemble to estimate the effect of fast dynamics on hopping rates. Three algorithms are implemented as described below and in Methods.

1) The fast limit, where the molecular rearrangement is much faster than the hole hopping time. This applies to the distributions calculated from the CPMD as the geometrical changes reported here cover up to 25 picoseconds. In this case, we make the approximation that the effective electronic coupling experienced by the hole on a given site is the square root of the average square electronic coupling (see Methods).

2) We assume that the molecular rearrangement is much slower than the hole hopping time. This is the static limit, where the dye lattice is frozen for the entire duration of the transport simulation. In practice this is equivalent to randomly assigning a value of electronic coupling (sampling the distributions generated with RMP) to every bond of the lattice at the beginning of the simulation and keeping it unchanged, providing us with a highly disordered lattice. We then use Boltzmann weighted probabilities for a charge to change site to simulate thermodynamic equilibrium (see

Methods).

3) We consider the intermediate regime where the molecular rearrangement happens on a similar time scale as the hole hopping. We treat this case by introducing a new parameter, the renewal time, t_{ren}, after which the electronic coupling of each bond of the lattice is randomly reassigned.[55] Here we use the distributions of J_{ij} for the pairs of dye generated with RMP (also using Boltzmann weighted CTRW). The fastest dynamics are neglected in this scenario (i.e we do not draw any J_{ij} from the CPMD generated distributions) and hence the kinetic Monte Carlo simulation is expected to underestimate the hole diffusion coefficient relative to the case where both large amplitude conformation changes and fast dynamics are included, as we show below.

For each charge transport simulation we track the mean square displacement, d_{rms} of the charge on the two dimensional lattice and calculate the diffusion coefficient, D_{calc}, from the variation of the average d_{rms} with respect to time (see Methods). The results are shown in Table 1.

Table 1: Diffusion coefficients calculated with the Continuous Time Random Walk algorithm (see Methods and figures in Supporting Information). For each dye we show the diffusion coefficient calculated with the calculated reorganisation energy.[56] The diffusion coefficients calculated with the *measured* reorganisation energy (which may include a contribution from disorder) are given in Supporting Information. The three cases (fast limit, static limit and intermediate regime) are separated by horizontal lines for clarity. The experimental data are shown for comparison where the measured apparent diffusion coefficient is converted into a two dimensional coefficient $D_{exp} = \frac{2}{3}D_{2D,exp}$, as extensively explained elsewhere[34] and in Supporting Information.

Case	$D_{calc,D102}$ / cm^2.s^{-1} with $\lambda_{calc} = 0.961$ eV	D_{D149} / cm^2.s^{-1} with $\lambda_{calc} = 0.896$ eV
Fast limit	4.5×10^{-7}	6.1×10^{-7}
Single value (reference)	1.5×10^{-7}	1.6×10^{-8}
Static limit	1.5×10^{-9}	1.7×10^{-8}
$t_{ren} = 10^{-1}$s	3.5×10^{-10}	3.5×10^{-8}
$t_{ren} = 10^{-3}$s	2.4×10^{-9}	3.8×10^{-8}
$t_{ren} = 10^{-5}$s	1.7×10^{-9}	4.5×10^{-8}
$t_{ren} = 10^{-6}$s	6.5×10^{-9}	5.3×10^{-8}
$t_{ren} = 10^{-7}$s	3.3×10^{-8}	9.2×10^{-8}
$D_{2D,exp}$	$9.6(\pm 2.0) \times 10^{-8}$	$2.5(\pm 0.8) \times 10^{-7}$

The fast limit (1), where we use the average of the square electronic coupling from the CPMD distribution, shows the highest diffusion coefficients. Within this limit the conformational disorder

is limited to small fluctuations around an upright, reasonably well coupled dye geometry; hence the hole moves faster across the lattice. The difference between the two dyes is washed out in this limit which is consistent with the observation that the average square electronic couplings are similar for both dyes, although the distributions of J_{ij} are different.

To examine the effect of these fast fluctuations on D_{calc} we also give the diffusion coefficient calculated with representative single values of J_{ij} for both lattice vectors direction (second line in Table 1). We choose, as a reference, the values at the peak of the distributions generated with CPMD (dotted line in Figure 4a to 4d). We observe that for D102 the difference between this J_{ij} and $\sqrt{< J_{ij}^2 >}$ is small (factor of 2) meaning that the fluctuations in J_{ij} caused by molecular vibrations have little impact on the diffusion coefficient. In contrast, for D149 the single value J_{ij} underestimates $\sqrt{< J_{ij}^2 >}$ by an order of magnitude. This is because the CPMD explores a larger space for D149 than for D102 within the time of the simulation as indicated by the broader distributions of J_{ij}^2. However we believe that in neither case does the CPMD explore the space that would be spanned by the dyes at longer times (microsecond). To study the effect of larger amplitude fluctuations we below use the distributions generated with RMP with a Boltzmann weighting, neglecting the fast fluctuations. Based on the comparison of typical J_{ij} and $\sqrt{< J_{ij}^2 >}$ for the CPMD case described above and previous studies[17] we infer that these simulations underestimate the diffusion coefficient by up to an order of magnitude.

The static limit (2) is the case where the disorder is maximal because the lattice is frozen and we logically obtain the lowest diffusion coefficients for both dyes in this limit. The difference between D_{calc} calculated for both dyes is the greatest.

The diffusion coefficient increases as the renewal time decreases. Indeed, after each time interval t_{ren}, the bonds of the lattice are reassigned with a different J_{ij}, drawn from the distribution. As a result, the charge is more likely to escape a weakly coupled site and moves faster across the lattice. The difference between the static limit and the longest renewal time ($t_{ren} = 10^{-1}$s) is not statistically meaningful as illustrated by the superposition of d_{rms} in Supporting Information. For D102 we see that the diffusion coefficient with the smallest renewal time (10^{-7}s) is 95 times higher

than the diffusion coefficient within the static limit. For D149, it is only 2.6 times higher. This can be rationalised looking at the J_{ij} distributions given in Figure 4 b and d. The distributions are much wider for D102 than they are for D149 which implies higher disorder. Therefore, the reassignment of the electronic coupling has more effect for D102 which explains the bigger increase in diffusion coefficient.

These results are consistent with other theoretical work done on organic semiconductors.[57,58] In particular, Geng et al. [57] noticed that the charge mobility was enhanced at room temperature by a phonon-assisted mechanism in a three dimensional molecular crystal. Although their study does not properly account for the relative timescale of charge transfer versus lattice fluctuations (the electronic coupling is systematically reassigned after each hop) their findings can be compared with our fast renewal time scenario. Then it seems that dynamical disorder helps charge conduction for both three dimensional organic semiconductors and our two dimensional dye monolayer. A study similar to Geng et al. s has also been done for one and two dimensional TIPS pentacene crystals.[58] Those authors observed that the effect of dynamical disorder on charge mobility depends on the dimensionality of the system. In particular, they report no influence of dynamical disorder on the charge mobility within the two dimensional crystals except in the case when the mean electronic coupling is less than its standard deviation. It would be interesting to see whether this is specific to the well defined herringbone crystal structure they studied or to the chemical structure of the molecule itself. In our case we have several distributions to account for the different configurations of the dyes in a disordered monolayer and, although not inconsistent, the same conclusions cannot be reached in a straightforward manner.

Experimental data are given here as guidance but suffer from limitations on their own due to the effect of series resistance which means that they also underestimate the diffusion coefficient as discussed in Supporting Information. Also, edges and grain boundaries of the TiO_2 nanoparticles are likely to affect the kinetics of charge transport.[10,59] However we believe that these features will not have a big effect here as each hole is likely to diffuse across only a fraction of a crystalline face of a nanoparticle before it is regenerated by the hole transporting medium. This is supported

by the transport simulations where the maximal mean square displacement of the charges on the simulated lattice can be compared with the surface area of a 10 nm radius TiO_2 nanoparticle. At most the mean square displacement represents 1.2% and 0.6% of the surface of one nanoparticle for D149 (in 0.5μs) and D102 (in 1μs) respectively (details given in Supporting Information). This implies that it is unlikely that one hole encounters a boundary or inter particle necking. Consequently we find interesting to see how our calculated diffusion coefficients compare with the measured ones. Because a straightforward comparison will still not be rigorous we focus here on the relative kinetics of the two dyes. We observe that it is the intermediate regime at short renewal time which reproduce the experimental trend best. The ratio of diffusion coefficient between the two dyes is consistent between calculated ($D_{D149,calc} \approx 2.7 D_{D102,calc}$) and measured ($D_{D149,exp} \approx 2.6 D_{D102,exp}$) values. This implies that the hole diffusion kinetics observed in real systems can be explained by a fast rearrangement of the molecules adsorbed on the TiO_2. This corroborates previous observations where the diffusion coefficient is seen to decrease when the viscosity of the surrounding hole transporting medium increases.[3,34,60] Indeed we expect a slower rearrangement of the molecular lattice in viscous environment and therefore, as demonstrated in this paper, a lower diffusion coefficient.

Although we believe that the anatase (101) surface is fully sensitised we cannot exclude the possibility of less than perfect coverage in the experimental systems. We also expect the renewal time t_{ren} to be temperature dependent in real systems. This could contribute to the measured activation energy of hole transport and might account for the larger experimental values relative to the simulation. Future work is underway which aim to quantify t_{ren} both theoretically and experimentally.

Concluding remarks

In this paper we have studied the influence of the configurational disorder within a dye molecule monolayer on the electronic coupling and the kinetics of hole transfer. We have considered the dy-

namic rearrangement of electronic couplings between dyes and their effect on a coupled transport simulation. We use a computationally efficient method of packing rigid dyes to represent different large amplitude fluctuations and evaluate the effect of fast dynamics by comparing dynamics of conformations for one configuration with those of a Car Parrinello Molecular Dynamics (CPMD) generated ensemble. We have compared our calculated diffusion coefficients to values measured experimentally and report a good agreement on the relative difference between the two indolene dyes considered. In particular we have observed that a static model cannot give a diffusion coefficient high enough to explain the experimental trend, as opposed to a model with a rearranging lattice. We conclude that it is likely to be the motion of the dyes on the surface that allows the fast conduction of holes through the monolayer. As a result, a greater range of configurational disorder will result in a slower hole transfer dynamics but can be balanced by a fast rearrangement of the molecules which allows charges to escape structurally trapping configurations. Consequently the viscosity of the medium surrounding the dyes is likely to play a role as it may slow the molecular dynamics. To design fast conducting molecular wires one needs to account for the freedom of the molecules once attached on the substrate.

Methods

Ab-initio Molecular Dynamics

Periodic DFT calculations have been carried out within the generalized gradient approximation (GGA) using the PBE exchange-correlation functional.[61] The Car-Parrinello (CP) model as implemented in Quantum-Espresso package was used.[62] Electron-ion interactions were described by ultrasoft pseudopotentials with electrons from S 3s, 3p; O, N and C 2s, 2p; H 1s; Ti 3s, 3p, 3d, 4s shells explicitly included in the calculations. Plane-wave basis set cutoffs for the smooth part of the wave functions and the augmented density were 25 and 200 Ry, respectively. The TiO_2 anatase (101) surface was modeled as a periodic slab with a thickness of ≈ 7 Å. As shown in Ref. 60, the computed binding energies are almost independent of the number of layers in the anatase

slabs.[63] The D102 and D149 pairs were adsorbed on one side of the slab. A minimum separation between repeated images of $\approx$ 10 Å was ensured throughout the simulation. The A and B periodic dimension of the TiO_2 slab were chosen to reproduce the two preferred adsorption positions along the x and y direction. Car-Parrinello molecular dynamics simulations have been carried out with an integration time step of 10 a.u.; the fictitious mass for the electronic degrees of freedom is 1000 a.u. and the atomic masses to the value of 5 amu.

Cell Parameters

D102 for the pair separated by $\mathbf{a}_{\mathrm{D102}}$: $A = 7.57$ Åand $B = 20.48$Å.

D102 for the pair separated by $\mathbf{b}_{\mathrm{D102}}$: $A = 15.14$Å$B = 10.24$ Å.

D149 for the pair separated by $\mathbf{a}_{\mathrm{D149}}$: $A = 11.35$ Å$B = 20.48$Å

D149 for the pair separated by $\mathbf{b}_{\mathrm{D149}}$: $A = 22.71$ Å$B = 10.24$Å.

Rigid Molecular Packing (RMP)

In PACKMOL, each atom or group of atoms can be constrained within a sphere or a box of user defined radius, centre, side length and angle. In this work we choose to place specific atoms (see details below) into spheres of very small radius to allow for minimal (with respect to the inter-atomic distance) but isotropic changes around the set absolute position (as illustrated in Figure 2 f. The specific set of constraints used to generate pairs of dyes mimicking their dynamical rearrangement on the surface are the following. Each oxygen atom from the carboxylic acid groups is constrained within a sphere of radius 0.01 Å which effectively fix the anchoring group in space while allowing the whole dye to adopt various inclination angles.

There are then 4 spheres to define for a pair (2 per dye). The centres of the two spheres from the same dye are separated by (2.2, 0.0, 0.0) so the oxygens are aligned along the x-direction.[38] This displacement (2.2 Å) is set to match the distance between the two oxygens in the optimised geometry of the dye. All atoms are set to be above the (0.0, 0.0, 1.0, 0.0) plane. The virtual surface is then in the (x,y) plane and its normal is carried along the positive z-direction. One carbon of the body of the dye is constrained within a box of size 20x20x8 Å. This is to ensure that the dyes do

not fall absolutely flat on the surface. The second dye of the pair is subject to the same constraints than the first dye but shifted by the displacements vectors in Figure 1. 450 pairs were created for each displacement vectors : 150 when the second dye in the pair is a simple translation of the first dye; 150 when the second dye is a simple translation but the first dye is then "flipped" around its anchoring feet; 150 when the second dye is first translated from the first dye and then "flipped" around its anchoring feet.

Electronic coupling

We make use of the frozen core orbital approximation and treat the electronic coupling, J_{ij}, between two molecules i and j as their HOMO overlap (for hole exchange). As described elsewhere,[48,52,53] J_{ij} can be found by reading the appropriate off-diagonal element of the following matrix :

$$(G^T B)^T \varepsilon_{pair} (G^T B), \tag{1}$$

where ε_{pair} are the eigenvalues of the pair of molecules; B is the basis of the normalised eigenvectors of the pair and $G = \begin{bmatrix} ... \Psi_k^i ... & 0 \\ 0 & ... \Psi_m^j ... \end{bmatrix}$ with Ψ_k^i (Ψ_m^j) the k^{th} (m^{th}) molecular orbital of the molecule i (j) expressed in the atomic orbitals basis set.

ε_{pair}, B, Ψ_k^i and Ψ_m^j are taken from three DFT energy calculations in vacuum (B3LYP/TZVP-6D with Gaussian09[64]) on the pair and each isolated molecules. All DFT calculations to get the electronic coupling are performed on the dyes without the TiO_2 surface but with protonated anchoring group. The hydrogen on the anchoring group aims to mimic the contribution from the surface to the HOMO of the dyes and allows both consistency between the CPMD and RMP generated pairs and savings on computational time. We test this approximation by comparing the electronic coupling between a pair of dyes anchored on a TiO_2 cluster and a pair of protonated dyes (see Supporting Information). We find $J_{Dye-H} \sim J_{Dye-TiO2}$ which validates our approach.

Continuous Time Random Walk[20,21]

We assume that the charge moves through the lattice by a succession of hops from one molecule to one of its nearest neighbours. The lattice reproduces the spacing of the dye molecules when anchored on the (101) TiO_2 surface (lattice vectors given in Figure 1).

The electronic coupling distributions are uniformly sampled to assign one J_{ij} to every lattice bond. In case 1 we sample the distributions from the CPMD generated pairs which obey thermodynamical equilibrium and do a random walk to extract diffusion coefficients. In cases 2 and 3, we also uniformly sample the distributions from the RMP generated pairs but perform a biased random walk to incorporate thermal equilibration effects (details in Supporting Information).

In case 2 where the molecular rearrangement is much slower than the hole hopping time, the electronic coupling between each possible lattice site is randomly fixed with values uniformly sampled from the distributions of possible J_{ij}. We use an adaptive time step, t_{wait}, defined as :

$$t_{wait} = -\frac{lnR}{\sum_{j=0}^{nn}\Gamma_{ij}}, \tag{2}$$

where R is a random number between 0 and 1, Γ_{ij} is the rate of intermolecular charge transfer between molecule i and molecule j and the summation is performed on all nearest neighbour (nn) pairs (here always 4 as shown in Figure 1).

The destination is picked according to the Boltzmann weighted distribution :

$$P_{ij} \propto \frac{\Gamma_{ij} \times exp\left(-\frac{\Delta U_{ij}}{k_B T}\right)}{\sum_{j=0}^{nn}\Gamma_{ij} \times exp\left(-\frac{\Delta U_{ij}}{k_B T}\right)}, \tag{3}$$

where P_{ij} is the probability of going from dye molecule i to dye molecule j and ΔU_{ij} is the energy difference between site j and site i when positive, it is set to 1 otherwise (details on the calculation of U_{ij} can be found in Supporting Information We use non-adiabatic Marcus theory in the weak coupling regime to define Γ_{ij}:

$$\Gamma_{ij} = \frac{2\pi}{\hbar}|J_{ij}|^2 \frac{1}{\sqrt{4\pi\lambda_{tot}k_BT}} \exp\left(-\frac{\lambda_{tot}}{4k_BT}\right), \quad (4)$$

where k_B is the Boltzmann constant, T the temperature, J_{ij} the electronic coupling between molecule i and j, λ_{tot} the total reorganisation of charge transfer and $\hbar$ is Planck's constant divided by 2π. Notice that we assume no energetic disorder ($\Delta G = 0$) since the charge donor and acceptor are identical.

The reorganisation energy of hole transfer is calculated via quantum chemical calculations using the four point energy method modified to incorporate solvent effects.[56] The electronic coupling is calculated as described above.

We calculate the diffusion coefficient, D_{calc} from the mean square displacement of the hole on the lattice:

$$D_{calc} = \frac{1}{4}\frac{< r^2 >}{\Delta t} \quad (5)$$

where $< r^2 >$ is the mean square displacement of the charge in the (xy) plane of the surface and Δt is the time step. Each walk is binned into 2000 smaller walks to improve statistics.

As described in Results and Discussion, in case 3 where the molecular rearrangement happens on a similar time scale as the hole hopping; the J_{ij} values are refreshed every t_{ren}.[55] More specifically, after each hop we calculate the waiting time according to Equation 2. Then we compare the waiting time to the renewal time. If $t_{wait} < t_{ren}$, the time is incremented by t_{wait}, the renewal time is decreased by t_{wait} and the charge changes site according to Equation 3. If $t_{wait} > t_{ren}$, the time is incremented by t_{ren}, new J_{ij} are assigned to the lattice bonds, a new waiting time is calculated accordingly and the procedure is reiterated. We note that if $t_{wait} > t_{ren}$ always, we never reach the condition for the charge to change site. Consequently, for a given distribution of electronic couplings, there is a minimum t_{ren} that one can simulate. In our case the threshold was $t_{ren} = 10^{-7}$s. Below this value, the charge is trapped on a site and never escapes.

For the case 1 where we assume that the charge sees an effective average electronic coupling,

we refine the definition of t_{wait} and P_{ij} :

$$t_{wait,CPMD} = -\frac{n_{tot} lnR}{\sum_{nn} \sum_{n_{tot}} \Gamma_{ij}}, \tag{6}$$

where n_{tot} is the total number of J_{ij} values we have in both directions and the summation of the rates is carried over the total distribution for all the nearest neighbour pairs. The destination site j is chosen randomly according to the probability distribution :

$$P_{ij,CPMD} \propto \frac{n_{tot} \sum_{n_{x\,\mathrm{or}\,y}} \Gamma_{ij}}{n_{x\,\mathrm{or}\,y} \sum_{nn} \sum_{n_{tot}} \Gamma_{ij}}, \tag{7}$$

where $n_{x\,\mathrm{or}\,y}$ is the number of J_{ij} in the distribution describing the pair aligned along the x or y direction, depending on the nearest neighbour pair considered.

The rest of the CTRW algorithm remains identical.

Acknowledgement

V. Vaissier was supported through a studentship in the Centre for Doctoral Training on Theory and Simulation of Materials at Imperial College funded by EPSRC under grant number EP/G036888/1. D. Moia was supported by EPSRC grant number EP/J002305/1. P. Barnes thanks the EPSRC for his career acceleration fellowship EP/J002305/1. J. Nelson thanks the Royal Society for a Wolfson Merit Award and the support from EPSRC grant number EP/K010298/1 and the Supergen program (EP/G031088/1). E. Mosconi, M. Pastore and F. De Angelis thank CNR Projects EFOR and RADIUS and FP7-ENERGY-2010 project 261920 ESCORT for financial support.

References

(1) O'Regan, B.; Grätzel, M. *Nature* **1991**, *353*, 737–739.

(2) Bach, U.; Lupo, D.; Comte, P.; Moser, J. E.; Weissortel, F.; Salbeck, J.; Spreitzer, H.; Grätzel, M. *Nature* **1998**, *395*, 583–585.

(3) Bonhôte, P.; Gogniat, E.; Tingry, S.; Barbé, C.; Vlachopoulos, N.; Lenzmann, F.; Comte, P.; Grätzel, M. *J. Phys. Chem. B* **1998**, *102*, 1498–1507.

(4) Yang, L.; Cappel, U. B.; Unger, E. L.; Karlsson, M.; Karlsson, K. M.; Gabrielsson, E.; Sun, L.; Boschloo, G.; Hagfeldt, A.; Johansson, E. M. J. *Phys. Chem. Chem. Phys.* **2011**, *14*, 779–789.

(5) Fillinger, A.; Parkinson, B. A. *J. Electrochem. Soc.* **1999**, *146*, 4559–4564.

(6) Weisspfennig, C. T.; Hollman, D. J.; Menelaou, C.; Stranks, S. D.; Joyce, H. J.; Johnston, M. B.; Snaith, H. J.; Herz, L. M. *Adv. Func. Mater.* **2014**, *24*, 668–677.

(7) Wang, Q.; Evans, N.; Zakeeruddin, S. M. *J. Am. Chem. Soc.* **2007**, *129*, 3163–3167.

(8) Ardo, S.; Meyer, G. J. *J. Am. Chem. Soc.* **2011**, *133*, 15384–15396.

(9) Mathijssen, S. G. J.; Smits, E. C. P.; van Hal, P. A.; Wondergem, H. J.; Ponomarenko, S. A.; Moser, A.; Resel, R.; Bobbert, P. A.; Kemerink, M.; Janssen, R. A. J.; de Leeuw, D. M. *Nat. Nanotechnol.* **2009**, *4*, 674–680.

(10) Hu, K.; Robson, K. C. D.; Beauvilliers, E. E.; Schott, E.; Zarate, X.; Arratia-Perez, R.; Berlinguette, C. P.; Meyer, G. J. *J. Am. Chem. Soc.* **2014**, *136*, 1034–1046.

(11) Song, W.; Ito, A.; Binstead, R. A.; Hanson, K.; Luo, H.; Brennaman, M. K.; Concepcion, J. J.; Meyer, T. J. *J. Am. Chem. Soc.* **2013**, *135*, 11587–11594.

(12) Trammell, S. A.; Yang, J.; Sykora, M.; Fleming, C. N.; Odobel, F.; Meyer, T. J. *J. Phys. Chem. B* **2001**, *105*, 8895–8904.

(13) Zhao, Y.; Swierk, J. R.; Megiatto, J. D. J.; Sherman, B.; Youngblood, W. J.; Qin, D.; Lentz, D. M.; Moore, A. L.; Moore, T. A.; Gust, D.; Mallouk, T. E. *Proceedings of the National Academy of Sciences of the United States of America* **2012**, *109*, 15612–15616.

(14) Soo, H. S.; Agiral, A.; Bachmeier, A.; Frei, H. *J. Am. Chem. Soc.* **2012**, *134*, 17104–17116.

(15) Swierk, J. R.; Mallouk, T. E. *Chem. Soc. Rev.* **2013**, *42*, 2357–2387.

(16) Rühle, V.; Kirkpatrick, J.; Andrienko, D. *J. Chem. Phys.* **2010**, *132*, 134103.

(17) Troisi, A.; Cheung, D.; Andrienko, D. *Phys. Rev. Lett.* **2009**, *102*, 116602.

(18) Troisi, A.; Ratner, M. A.; Zimmt, M. B. *J. Am. Chem. Soc.* **2004**, *126*, 2215–2224.

(19) Car, R. *Phys. Rev. Lett.* **1985**, *55*, 2471–2474.

(20) Kenkre, V. M.; Montroll, E. W.; Shlesinger, M. F. *J. Stat. Phys.* **1973**, *9*, 45–50.

(21) Montroll, E. W.; W, E.; Scher, H. *J. Stat. Phys.* **1973**, *9*, 101–135.

(22) Cramer, T.; Steinbrecher, T.; Labahn, A.; Koslowski, T. *Phys. Chem. Chem. Phys.* **2005**, *7*, 4039–4050.

(23) Skourtis, S. S.; Balabin, I. A.; Kawatsu, T.; Beratan, D. N. *Proceedings of the National Academy of Sciences* **2005**, *102*, 3552–3557.

(24) Kawatsu, T.; Beratan, D. N.; Kakitani, T. *J. Phys. Chem. B* **2006**, *110*, 5747–5757.

(25) Grozema, F. C.; Tonzani, S.; Berlin, Y. A.; Schatz, G. C.; Siebbeles, L. D. A.; Ratner, M. A. *J. Am. Chem. Soc.* **2008**, *130*, 5157–5166.

(26) Gutierrez, R.; Caetano, R.; Woiczikowski, P. B.; Kubar, T.; Elstner, M.; Cuniberti, G. *arXiv.org* **2009**,

(27) Castner, E. W.; Kennedy, D.; Cave, R. J. *J. Phys. Chem. A* **2000**, *104*, 2869–2885.

(28) Vukmirović, N.; Wang, L.-W. *Nano Lett.* **2009**, *9*, 3996–4000.

(29) Noriega, R.; Salleo, A.; Spakowitz, A. J. *Proceedings of the National Academy of Sciences* **2013**, *110*, 16315–16320.

(30) Senthilkumar, K.; Grozema, F. C.; Bickelhaupt, F. M.; Siebbeles, L. D. A. *J. Chem. Phys.* **2003**, *119*, 9809–9817.

(31) Vehoff, T.; Chung, Y. S.; Johnston, K.; Troisi, A.; Yoon, D. Y.; Andrienko, D. *J. Phys. Chem. C* **2010**, *114*, 10592–10597.

(32) Fornari, R. P.; Troisi, A. *Phys. Chem. Chem. Phys.* **2014**,

(33) Ciuchi, S.; Fratini, S.; Mayou, D. *Phys. Rev. B* **2011**, *83*, 081202.

(34) Moia, D.; Vaissier, V.; López-Duarte, I.; Torres, T.; Nazeeruddin, M. K.; O'Regan, B. C.; Nelson, J.; Barnes, P. R. F. *Chem. Sci.* **2014**, *5*, 281–290.

(35) Ding, I.-K.; Tétreault, N.; Brillet, J.; Hardin, B. E.; Smith, E. H.; Rosenthal, S. J.; Sauvage, F.; Grätzel, M.; McGehee, M. D. *Adv. Func. Mater.* **2009**, *19*, 2431–2436.

(36) Snaith, H. J.; Petrozza, A.; Ito, S.; Miura, H. *Adv. Func. Mater.* **2009**, *19*, 1810–1818.

(37) Fattori, A.; Peter, L. M.; Wang, H.; Miura, H.; Marken, F. *J. Phys. Chem. C* **2010**, *114*, 11822–11828.

(38) Pastore, M.; Angelis, F. D. *ACS Nano* **2010**, *4*, 556–562.

(39) Pastore, M.; Angelis, F. D. *J. Phys. Chem. Lett.* **2011**, *2*, 1261–1267.

(40) Nunzi, F.; Storchi, L.; Manca, M.; Giannuzzi, R.; Gigli, G.; De Angelis, F. *ACS Appl. Mater. Interfaces* **2014**, 140217084623003.

(41) Vittadini, A.; Selloni, A.; Rotzinger, F. P.; Grätzel, M. *Phys. Rev. Lett.* **1998**, *81*, 2954–2957.

(42) Pastore, M.; De Angelis, F. *Phys. Chem. Chem. Phys.* **2011**, *14*, 920–928.

(43) Pastore, M.; De Angelis, F. *J. Phys. Chem. Lett.* **2013**, *4*, 956–974.

(44) Li, X.; Nazeeruddin, M. K.; Thelakkat, M.; Barnes, P. R. F.; Vilar, R.; Durrant, J. R. *Phys. Chem. Chem. Phys.* **2011**, *13*, 1575–1584.

(45) Howie, W. H.; Claeyssens, F.; Miura, H.; Peter, L. M. *J. Am. Chem. Soc.* **2008**, *130*, 1367–1375.

(46) Martínez, L.; Andrade, R.; Birgin, E. G. *Comput. Chem.* **2009**, *30*, 2157–2164.

(47) Martínez, J. M.; Martínez, L. *Comput. Chem.* **2003**, *24*, 819–825.

(48) Valeev, E. F.; Coropceanu, V.; da Silva Filho, D. A.; Salman, S.; Brédas, J.-L. *J. Am. Chem. Soc.* **2006**, *128*, 9882–9886.

(49) Bredas, J. L.; Beljonne, D.; Coropceanu, V.; Cornil, J. *Chem. Rev.* **2004**, *104*, 4971–5003.

(50) Coropceanu, V.; Cornil, J.; da Silva Filho, D. A.; Olivier, Y.; Silbey, R.; Brédas, J.-L. *Chem. Rev.* **2007**, *107*, 926–952.

(51) Pietro, W. J.; Marks, T. J.; Ratner, M. A. *J. Am. Chem. Soc.* **1985**, *107*, 5387–5391.

(52) Kirkpatrick, J. *Int. J. Quant. Chem.* **2007**, *108*, 51–56.

(53) Senthilkumar, K.; Grozema, F. C.; Bickelhaupt, F. M.; Siebbeles, L. D. A. *J. Chem. Phys.* **2003**, *119*, 9809–9817.

(54) Nelson, J.; Kwiatkowski, J. J.; Kirkpatrick, J.; Frost, J. M. *Acc. Chem. Res.* **2009**, *42*, 1768–1778.

(55) Druger, S. D.; Nitzan, A.; Ratner, M. A. *J. Chem. Phys.* **1983**, *79*, 3133.

(56) Vaissier, V.; Barnes, P.; Kirkpatrick, J.; Nelson, J. *Phys. Chem. Chem. Phys.* **2013**, *15*, 4804–4814.

(57) Geng, H.; Peng, Q.; Wang, L.; Li, H.; Liao, Y.; Ma, Z.; Shuai, Z. *Adv. Mater.* **2012**, *24*, 3568–3572.

(58) Wang, L.; Li, Q.; Shuai, Z.; Chen, L.; Shi, Q. *Phys. Chem. Chem. Phys.* **2010**, *12*, 3309–3314.

(59) Van de Lagemaat, J.; Benkstein, K. D.; Frank, A. J. *J. Phys. Chem. B* **2001**, *105*, 12433–12436.

(60) Wang, Q.; Zakeeruddin, S. M.; Nazeeruddin, M. K.; Humphry-Baker, R.; Grätzel, M. *J. Am. Chem. Soc.* **2006**, *128*, 4446–4452.

(61) Perdew, J. P.; Burke, K.; Ernzerhof, M. *Phys. Rev. Lett.* **1996**, *77*, 3865–3868.

(62) Giannozzi, P. et al. *J . Phys. Cond. Matter* **2009**, *21*, 395502.

(63) Martsinovich, N.; Jones, D. R.; Troisi, A. *J. Phys. Chem. C* **2010**, *114*, 22659–22670.

(64) Frisch, M. J. et al. Gaussian 09 Revision D.01. Gaussian Inc. Wallingford CT 2009.

Supporting Information Available

Experimental methods

The experimental method used to measure D_{exp} is described in details elsewhere.[34] Here we report the main points regarding such procedure. We also comment on the correction of the values that we report in the main text on the basis of non idealities which are found to have an important role in our measurements.

Samples preparation Fluorine tin oxide (FTO) conductive TEC-15 glass substrates were used. The cleaning procedure consisted in washing the slides with soap and rinsing them with deionised water, acetone and isopropanol. They were finally heated to 450 °C for 30 minutes. TiO_2 paste (Dyesol 18 NR-T) was applied on the substrates via doctor blading. By sintering the samples (450 °C for 30 minutes adopting 10 minute heating ramp), TiO_2 films of about 7 μm thickness (d) were obtained. Dyeing of the films was performed by immersing the samples in dye solution (0.1 mM D102 or 0.06 mM D149 both in 1:1 volume ratio of acetonitrile:tert-butyl alcohol) directly from the oven were they were stored at a temperature of 120 °C. Two dyeing times were considered: a relatively short time (3.5 hours) as short time dyeing is often adopted when fabricating solid state DSSCs; dyeing time of 20 hours was also performed, as full coverage is desirable when comparing experimental data to computed values of the diffusion coefficient. Before measuring

the films, they were rinsed in acetonitrile for 1 to 5 minutes and then inserted in an electrochemical cell.

Experimental setup Cyclic voltammetry was performed by means of an IVIUM CompactStat instrument. The dye sensitised films were used as working electrode of the cell. A silver/silver chloride (3M NaCl) reference electrode and a platinum counter electrode were used to complete the three electrode configuration. All measurements were performed in 0.1 M tert butyl ammonium perchlorate (TBAP) dissolved in acetonitrile. By scanning the potential of the working electrode (dye sensitised film) towards positive electrochemical potential, oxidation of the dyes in proximity of the FTO substrate occurs. The hole injected in the dye is then able to hop to other molecules resulting in a diffusion limited current across the depth of the film.

Method The redox potential related to the oxidation of the dyes anchored to the TiO_2 was estimated (Eredox) by setting the scan rate (ν) to 50 mV/s and taking the average of the oxidation and reduction peaks of the cyclic voltammogram. For the estimation of the apparent diffusion coefficient (D_{exp} in the main text), higher values of scan rate (between 0.2 and 0.5 V/s) were adopted. D_{exp} was calculated from the current density peak j_p (A cm^{-2}) and the dye loading c_0 (cm^{-3}) as follow :

$$D_{exp} = 5.02 \frac{k_B T j_p^2}{q^3 c_0^2 \nu} \tag{8}$$

where q is the charge of an electron, k_B is the Boltzmann constant, T is temperature.

$D_{2D,exp}$ reported in the text is obtained by using the relationship $D_{exp} = \alpha D_{2D,exp}$, where α accounts for the dimensionality of the dye monolayer. For the surface of the mesoporous TiO_2 film we expect $\alpha < \frac{2}{3}$. Here, we use a value of α of $\frac{2}{3}$ which approximates the dimensionality of the system to be 3. This corresponds to approximating the system under study to an isotropic three dimensional lattice.

In table S1 we report the values of c_0 (measured via UV-vis absorption of the sensitised film) and of D_{exp} obtained for the two materials under different dyeing conditions. Table S1.

Discussion of the effect of series resistance

Table 2: Values of dye loading and of hole apparent diffusion coefficient measured for D102 and D149 sensitized TiO_2 films. D_{exp} was extracted from cyclic voltammograms of 3 or more samples using Equation 8. c_0 was extracted from the absorption spectrum of a 1μm thick film that was dyed in the same vial as the samples used for electrochemical measurement by using Beer Lambert's law.

	D102		D149	
	D_{exp} / 10^{-7}cm^2.s^{-1}	c_0 / cm^{-3}	D_{exp} / 10^{-7}cm^2.s^{-1}	c_0 / cm^{-3}
$t_{dyeing} = 3.5$ hrs	0.62 ± 0.27	6.13 ± 1.0	1.7 ± 0.2	6.0 ± 0.9
$t_{dyeing} = 20$ hrs	0.63 ± 0.12	9.2 ± 1.4	1.9 ± 0.3	6.9 ± 1.1

For diffusion limited cyclic voltammograms, the current density peak resulting from the measurement is proportional to $\nu^{1/2}$. Low values of scan rate are desirable in that when low current and low current density are to be measured the effects of respectively series resistance and kinetic limitation at the FTO/dyed TiO_2 interface (that we indicate as $x = 0$) can be neglected. However, the value of ν needs to be high enough so that during the measurement and up to when the current density peak is reached, a negligible fraction of dyes at the end of the film ($x = d$) is in the oxidised state. When both these conditions are met, and only for single electron reactions, the apparent diffusion coefficient can be estimated with Equation 8. We find that in our experimental procedure, for dyes with high ($D_{exp} \geq 3 \times 10^{-8}$cm^2.$s^{-1}$) diffusion coefficient, the effect of series resistance and of the finite rate of charge transfer at the FTO/dyed TiO_2 interface becomes significant. Both D102 and D149 belong to this category and we expect the error in the determination of D_{exp} by using Equation 8 to be dominant when compared to other experimental errors. If the series resistance of the cell (FTO and electrolyte) were negligible and the equilibrium between the FTO contact and the dyes at the interface were guaranteed throughout the experiment, then the electrochemical potential $E(t)$ of the dyes at $x = 0$ can be defined as:

$$E(t) = E(t = 0) + \nu t \tag{9}$$

As a result of the relatively high diffusion coefficient of holes transported across the dyes, the current density recorded is such that the conductivity of the components that set the dyes' electrochemical potential is limiting. This leads to:

$$E(t) = E(t=0) + \nu t - \Delta V(t) \tag{10}$$

where $\Delta V(t)$ accounts for the potential needed to drive the current in the system.

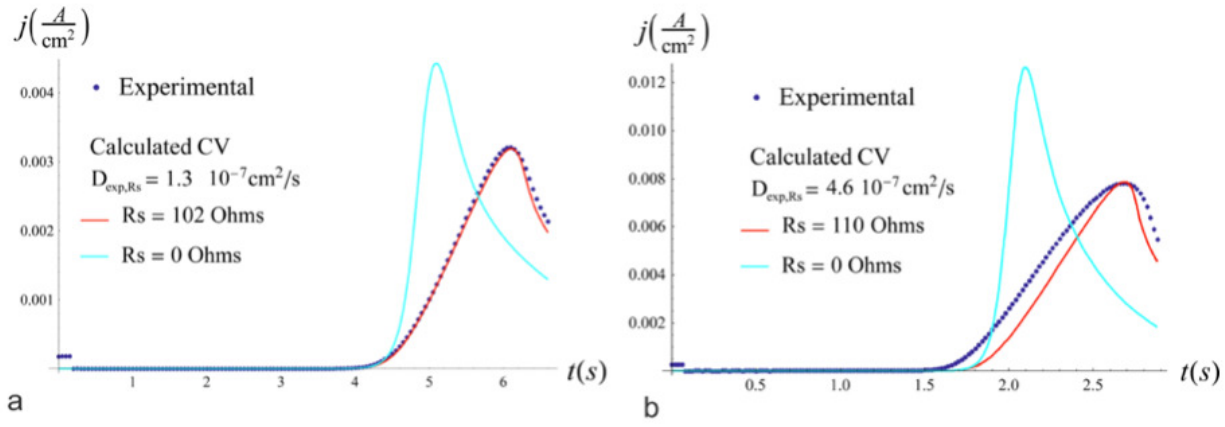

Figure 5: Experimental current density versus time (blue dotted line) measured with cyclic voltammetry and relative calculated curves for D102 (a) and D149 (b) sensitised TiO_2 films on FTO substrates. The red lines represent calculated curves where an effective series resistance (R_s) is included in the model when defining the boundary condition at the FTO/dyed TiO_2 interface. The value of D_{exp} and R_s are varied in order to match the current density peak and the peak position.

In Figure 5 we plot the current density measured with cyclic voltammetry on a D102 (a) and a D149 (b) sensitised TiO_2 mesoporous film on FTO versus time. Scan rate values of 0.2 V/s for D102 and 0.5 V/s for D149 have been used to comply with the semi-infinite slab approximation that we described earlier in this document. The red and cyan lines are obtained from calculation as described below. The red lines in Figure 5 are obtained by numerically solving Fick's first law of diffusion and using Equation 10 as boundary condition at the FTO/dyed TiO_2 interface, with $\Delta V(t)$ being:

$$\Delta V(t) = R_s I(t) \tag{11}$$

The values of R_s and D_{exp} are such to reproduce at the same time the current density peak and the peak position. Their values is therefore not a result of a fit over the whole set of data. Each of

the cyan lines represents another calculated curve using the estimated value of D_{exp} but adopting Equation 9 as boundary condition. This is what one would expect for an equally "fast" diffusion of the holes but in the absence of series resistance. We observe that data collected for D102 can be reasonably explained by including the effect of R_s in the model. Conversely, data for D149 show a broader shape of the cyclic voltammogram which we are not able to explain. This effect could be due to the particular way the dye packs on the surface or to a multiple electron redox exchange. We also notice that D149 sensitized films undergo more pronounced desorption during the measurement than D102 or other dyes we have tested. The desorption of oxidized dyes would indeed have a time dependent influence on the diffusion of holes within the remaining dyes in the monolayer. The values obtained by simply applying Equation 8 to the measurements shown in Figure 5 (D_{exp}) and the ones resulting from our analysis (D_{exp,R_s}) are listed in Table 3.

Table 3

	D_{exp} / cm^2.s^{-1}	D_{exp,R_s} / cm^2.s^{-1}	Ratio $\frac{D_{exp}}{D_{exp,R_s}}$
D102 sample	0.69×10^{-7}	1.3×10^{-7}	0.53
D149 sample	1.8×10^{-7}	4.6×10^{-7}	0.39

This analysis is aimed to give a sense of the error committed when using Equation 8 to estimate the diffusion coefficient of holes in dye sensitized systems. Values reported for D149 and D102 in the main text are meant to define the order of magnitude of the actual diffusion coefficient and to be used for comparison between the two dyes.

Comments on the kintetics at the interface In the case where also kinetic limitations at the FTO/dyed TiO_2 interface are considered, $\Delta V(t)$ can be expressed as:

$$\Delta V(t) = R_s I(t) + \frac{k_B T}{0.5} \text{arcsinh}\left(\frac{j(t)}{j_0}\right) \tag{12}$$

Here, in addition to the effect of series resistance, an overpotential is considered. The expression of this component is derived from the Butler-Volmer equation using j_0 as the exchange current density and a value of 0.5 for the Butler-Volmer charge transfer coefficient. When using Equation 12 to express $\Delta V(t)$ in the model, multiple sets of values for the parameters D_{exp}, R_s, and j_0 en-

able accurate match of the peak as described earlier. Despite the additional free parameter, we are not able to reproduce the broadening of the cyclic voltammograms of D149 sensitised samples. Furthermore, the values of D_{exp} extracted from this analysis when using only contribution from R_s (very high j_0) are highest. Therefore, we can consider the ratios expressed in Table **??** as an upper limit of the degree of underestimation of the actual value D_{exp} when using Equation 8.

Additional simulations

HOMO localisation on D102 and D149

Figure 6 gives an illustration of the localisation of the Highest Occupied Molecular Orbital (HOMO) in indolene dyes.

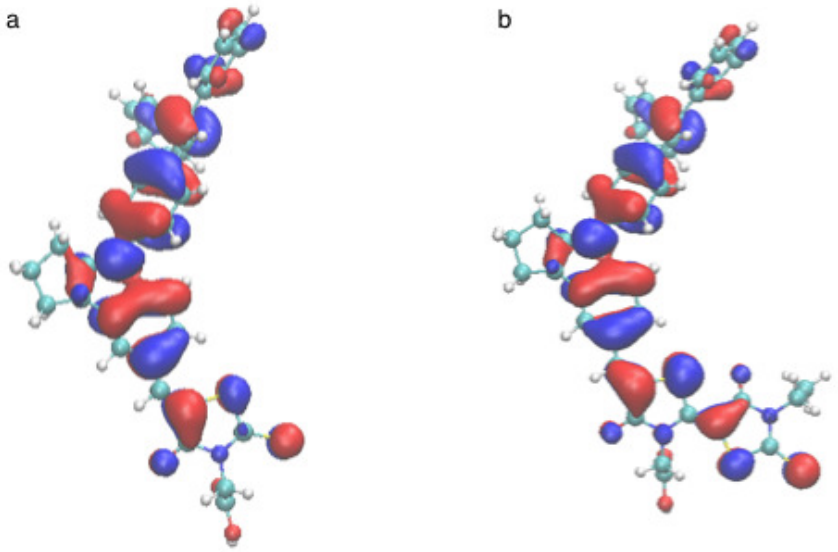

Figure 6: HOMO localization on D102 (a) and D149 (b) from DFT calculations (B3LYP/TZVP-6D, Gaussian09) (isovalues of 0.02 and -0.02).

Influence of the TiO_2 surface on the electronic coupling

We check the effect on J_{ij} of replacing the TiO_2 surface by an hydrogen atom as follows. First we create a highly symmetric pair of protonated D102 dyes (cf. Figure 7a) for which we calculate

the electronic coupling with the projective method : $J_{ij} = 0.382$ meV. Because the dyes are perfect mirror image of one another the coupling can also be found by looking at half the HOMO energy difference of the dimer. Here we get $J_{HOMO-splitting} = 0.380$meV. This certifies that our implementation of the projective method is correct; hence that our values of J_{ij} can be trusted. Second, we take the same pair of dyes but substitute a TiO_2 slab to the hydrogen of the anchoring group (see Figure 7b). We calculate the coupling with the projective method and obtain $J_{ij} = 0.346$meV which is very close to the value from the pair without the surface. This validates the approximation of using protonated dyes for J_{ij} calculations in this study. It has to be noted that in this case the HOMO splitting energy difference has no physical meaning. Indeed the complex generated is purely hypothetical with a necessarily disconnected surface slab to ensure perfect symmetry of the dyes. Additionally the lack of periodic boundary conditions in Gaussian 09 DFT calculations with localised basis sets makes the energy levels of the pair unreliable.

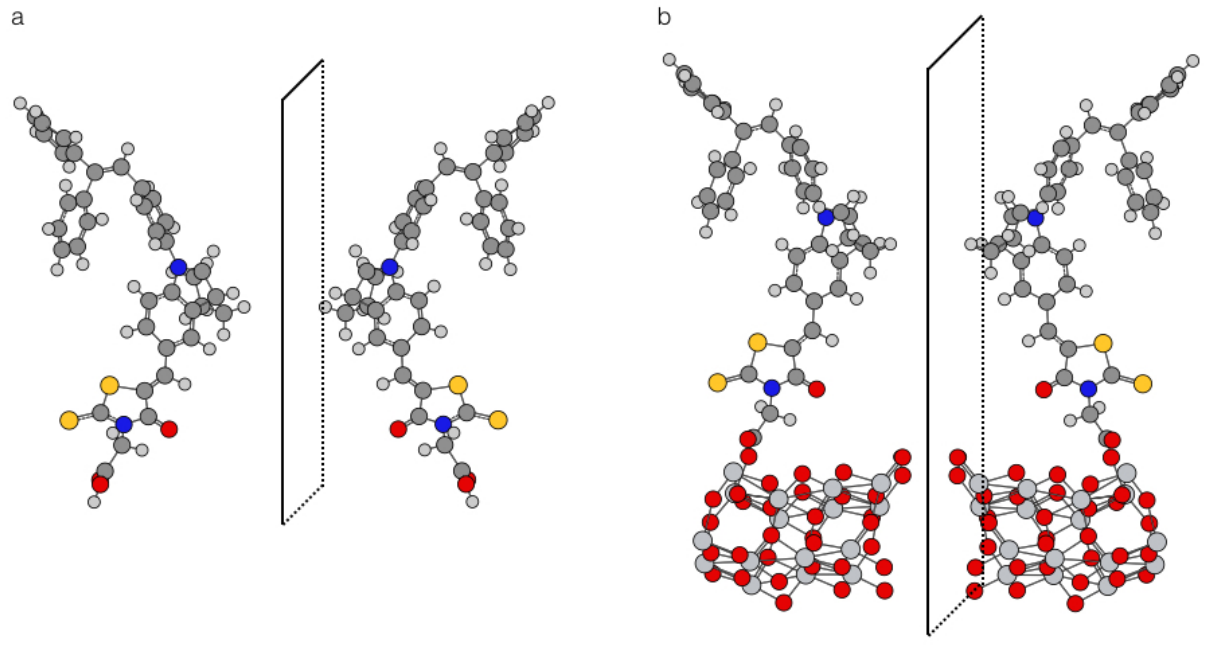

Figure 7: Symmetric complexes generated to test the validity of using protonated dye molecules for the calculation of the electronic coupling. (a) Pair of protonated D102 mirror image of one another. (b) Same pair of D102 as in (a) where the hydrogen of the anchoring group is replaced by a TiO_2 cluster.

Additional characteristics of the electronic coupling distributions

The average of the electronic coupling from the distributions shown in Figure 4 is given in Table 4.

Table 4: Average of the electronic coupling and average of the square electronic coupling for D102 and D149 for the distributions illustrated in Figure 4.

Case	$< J_{ij} >$ / eV	$< J_{ij}^2 >$/ eV^2
Packmol total x D102	3.250×10^{-2}	5.264×10^{-3}
Packmol total y D102	2.650×10^{-3}	2.590×10^{-4}
Packmol total x D149	1.124×10^{-2}	7.100×10^{-4}
Packmol total y D149	4.792×10^{-3}	2.633×10^{-4}
CPMD x D102	5.193×10^{-3}	7.213×10^{-5}
CPMD y D102	2.356×10^{-3}	1.419×10^{-5}

Figure 8 shows the evolution of the electronic coupling as a function of the time simulated with CPMD.

We observe that the distributions are centred around the $J_{ij} = 0$ as expected. The magnitude of the variations are analysed in the main text.

Pair energies from Universal Force Field (UFF) calculations

Figures 9 and 10 show the correlation between the electronic coupling and the energies (u_{ij}) for each RMP generated pairs. The energy is the sum of the Coulomb and Van der Waals interactions calculated with Universal Force Field (UFF) in Gaussian 09.

From these results we can define the energy at a given site i as :

$$U_i = \frac{1}{2} \sum_{j=0}^{nn} u_{ij}, \tag{13}$$

where u_{ij} is the energy of the pair calculated with UFF.

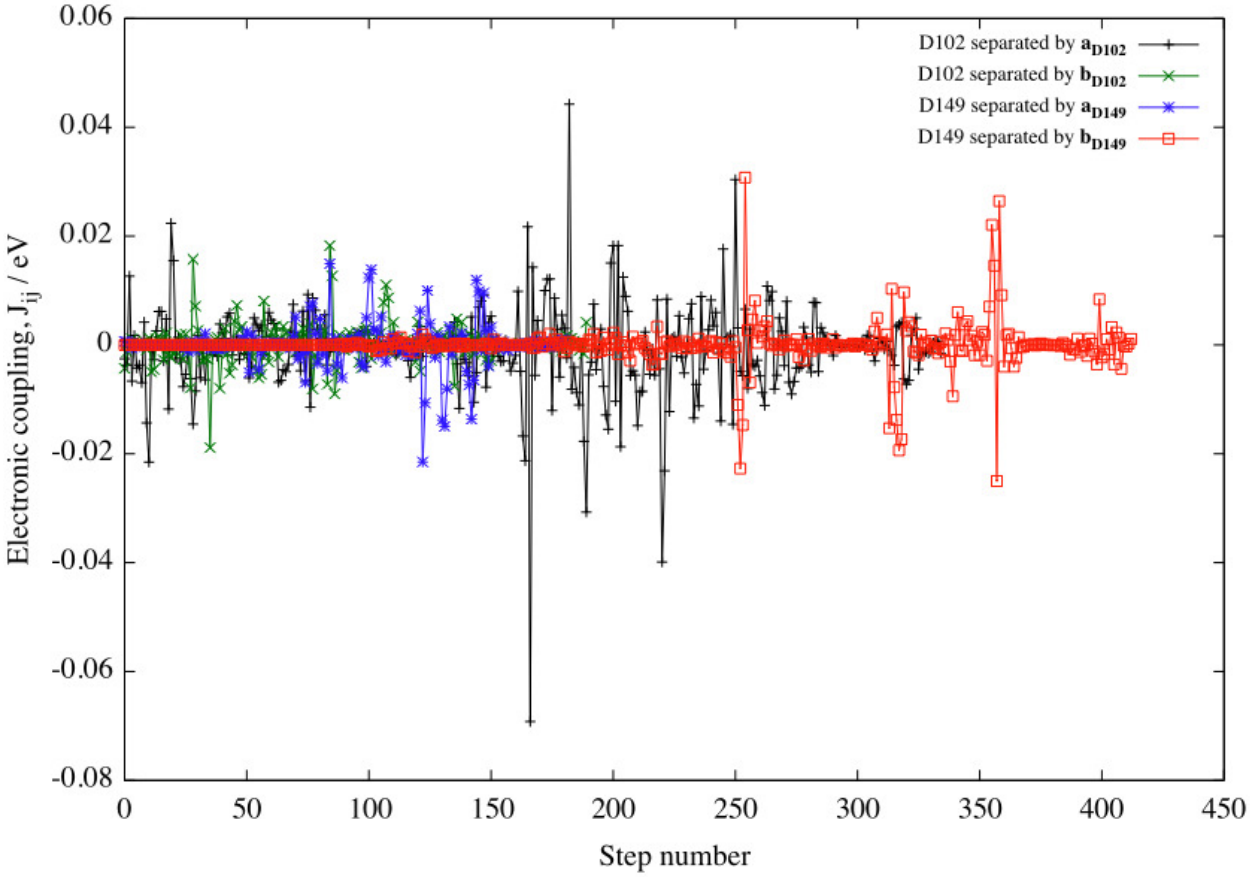

Figure 8: Evolution of the electronic coupling over the CPMD trajectories for D102 and D149 in both directions. The x-axis is the CPMD simulation step number which can be readily converted into time given the time step, $\Delta t = 0.048$ps.

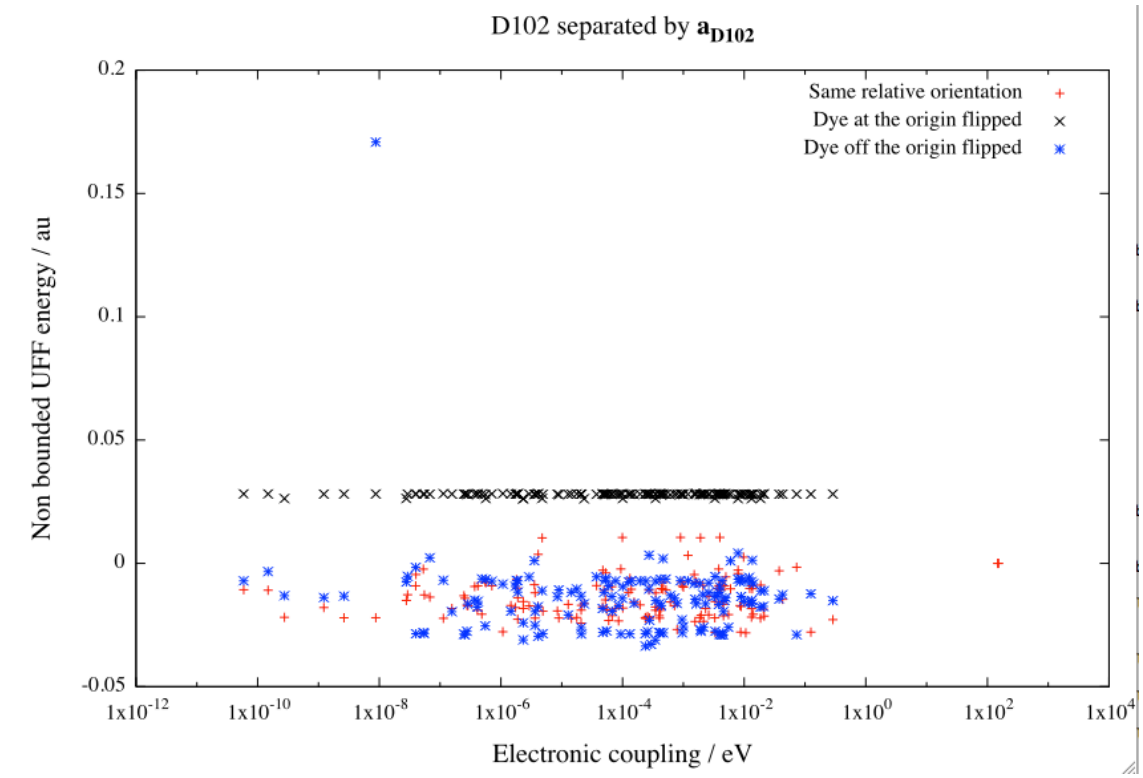

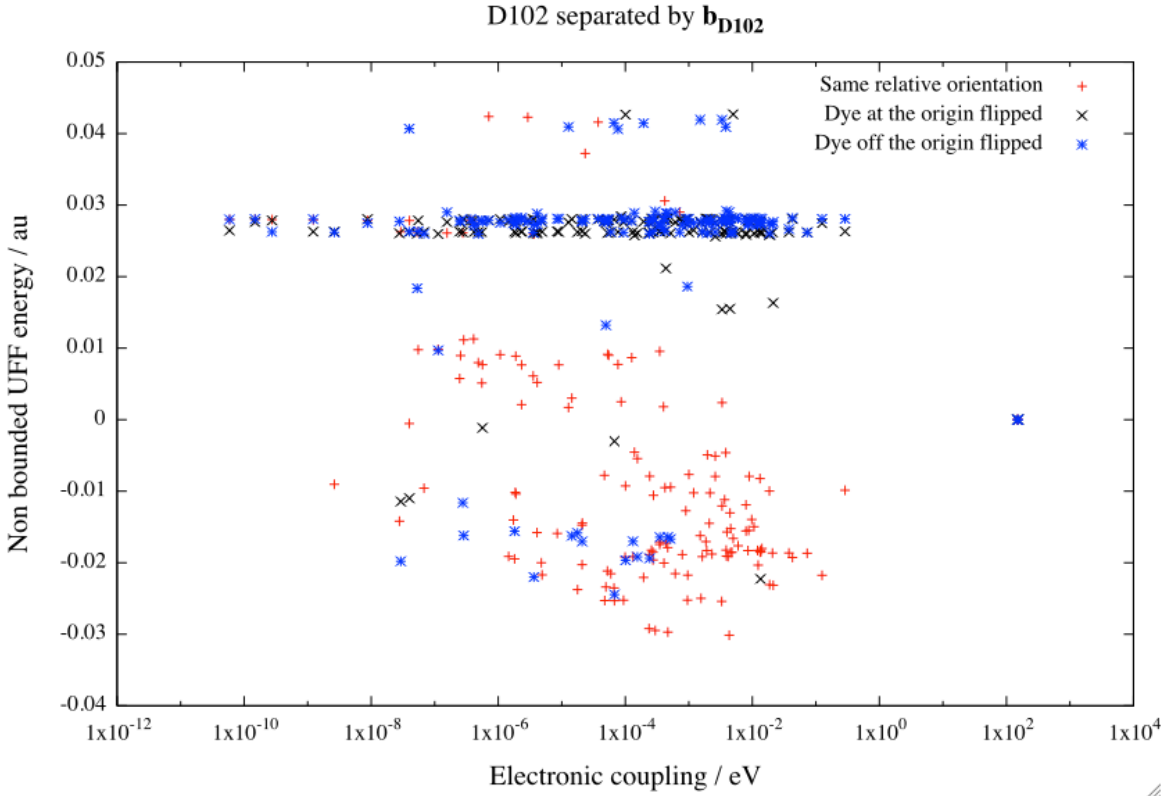

Figure 9: Non bounded interaction energy for D102 pairs. The energy is the sum of the Coulomb and Van der Waals interactions calculated with Universal Force Field (UFF) in Gaussian 09.

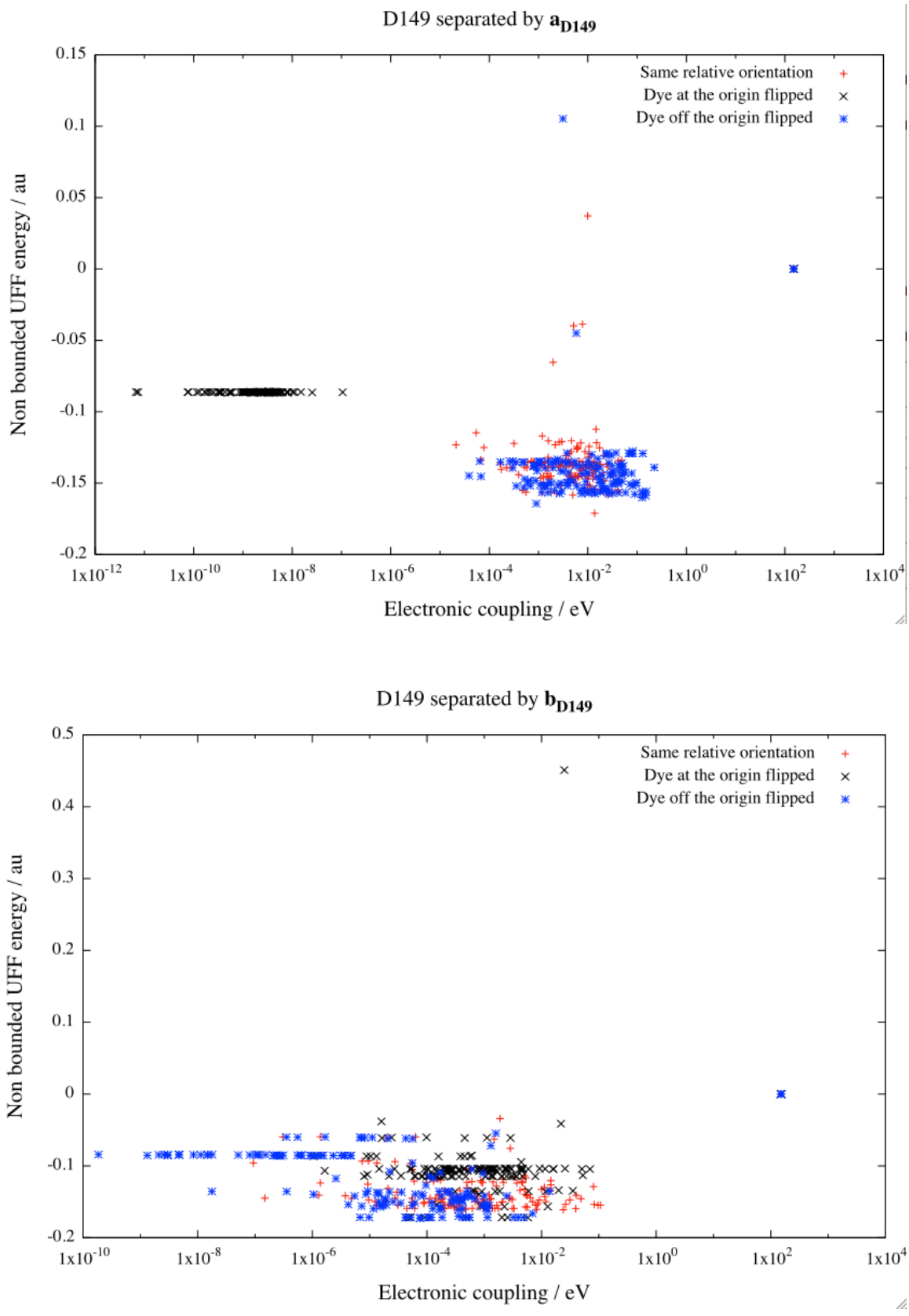

Figure 10: Non bounded interaction energy for D149 pairs. The energy is the sum of the Coulomb and Van der Waals interactions calculated with Universal Force Field (UFF) in Gaussian 09.

RMP generated lattice thermal equilibration

As mentioned in the main text, the RMP generated J_{ij} distributions do not satisfy thermodynamic equilibrium. To assess how far a random lattice is from thermal equilibrium we build an Ising relaxation scheme :

step 1 : build a lattice for which one J_{ij} and its corresponding energy (u_{ij}) are randomly assigned to every bond.

- step 2 : pick a site at random and calculate its energy according to Equation 13 $U_{i,old}$

- step 3 : reassign (J_{ij}, u_{ij}) to the four bonds of the site and calculate the new site energy, $U_{i,new}$

- step 4: if $\Delta U = U_{i,new} - U_{i,old} < 0$ accept the changes and go back to step 1.

Else only accept the change if X, random number between 0 and 1 is below the Boltzmann factor associated with the change ($exp\left(-\frac{\Delta U}{k_B T}\right)$) and go back to step 1.

The energy variation of two 30 by 30 D102 and D149 lattices is given in Figure 11.

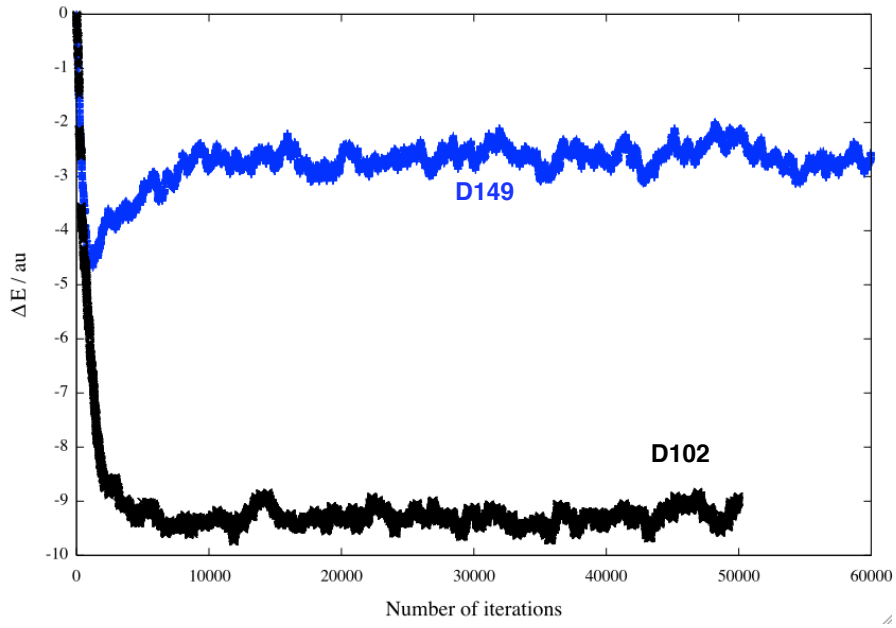

Figure 11: Total energy variation of randomly generated D102 and D149 lattices (30*30 sites) following thermal relaxation according to an Ising scheme.

The energy difference between the starting lattice and the lattice at convergence, normalised by the number of sites is about 3 and 10 k_BT for D149 and D102 respectively. This implies that a randomly generated lattice is too far from equilibrium to neglect thermal relaxation effects. However these equilibrations are quite expensive. Hence we use rather small lattices. We test our procedure with respect to the lattice size and obtain the expected linear relationship between the lattice energy at convergence and the number of sites, as shown in Figure 12. As can be observed our biggest lattice here is 100*100 sites which we believe is too small to perform a random walk on. This study stresses the importance of thermal equilibration for the RMP generated lattice but bigger lattices are required to get good statistics on the diffusion coefficients. To resolve this issue we do a biased random walk on the initial lattices to incorporate thermodynamics effects. In other words, the sampling of the molecular pairs will be weighted by a Boltzmann distributed sampling of the pair energies.

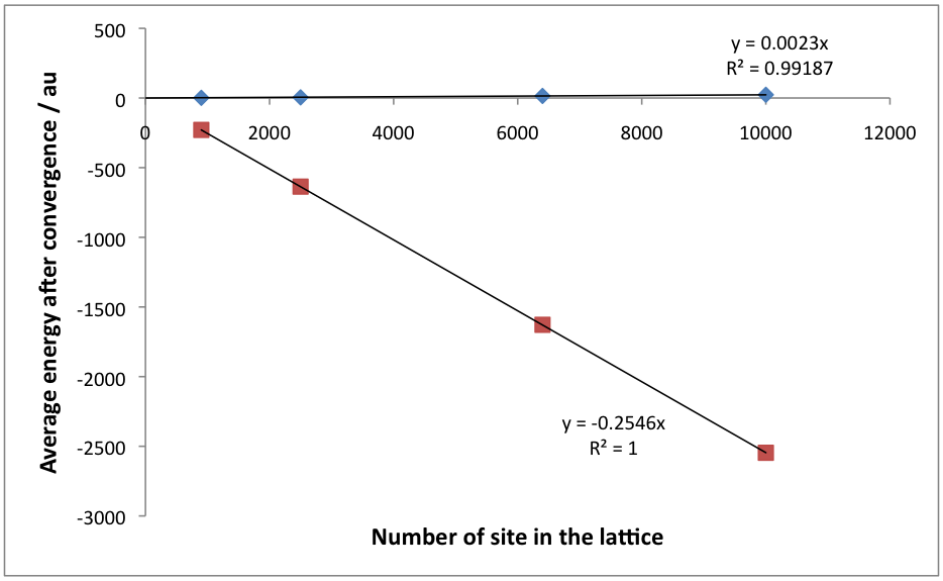

Figure 12: Total lattice energy at convergence as a function of the number of sites for D102 and D149 RMP generated lattice.

Random walks and diffusion coefficients

Figure 13 shows the walks for D102 and D149 in case 3. The mean square displacement reaches 8×10^{-14} and 1.5×10^{-13} cm^2 at the most for D102 and D149 respectively. The surface area of a

TiO_2 nanoparticle of radius 10 nm, (assumed spherical) is about 1.26×10^{-11} cm^2. Hence a charge diffuses across 0.64 and 1.2 % of a TiO_2 nanoparticle for D102 and D149 respectively. This implies that, at first approximation, we can neglect the effects of the edges and grain boundaries in the mesoporous film when comparing with experimental data.

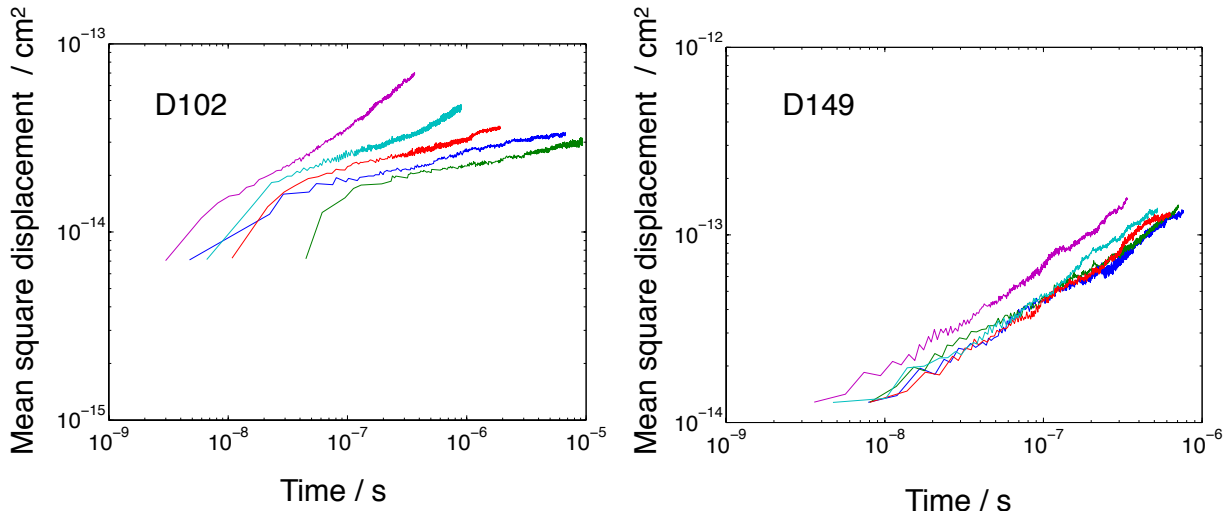

Figure 13: Mean square displacement of the charge on the RMP generated D102 and D149 lattices as simulated with the biased random walk in case 3. The runs from different renewal time are superimposed in both cases. The colour code is as follows : green : $t_{ren} = 10^{-1}$s, dark blue : $t_{ren} = 10^{-3}$s, red : $t_{ren} = 10^{-5}$s, cyan : $t_{ren} = 10^{-6}$s, magenta : $t_{ren} = 10^{-7}$s.

Table 5: Diffusion coefficients calculated with the Continuous Time Random Walk algorithm with the calculated the measured reorganisation energy.

Case	D_{D102} / cm^2.s^{-1} with $\lambda_{exp} = 1.336$ eV	D_{D149} / cm^2.s^{-1} with $\lambda_{exp} = 1.023$eV
Fast limit	2.60×10^{-7}	5.08×10^{-7}
Static limit	8.98×10^{-10}	1.41×10^{-8}
$t_{ren} = 10^{-1}$s	6.12×10^{-10}	1.19×10^{-8}
$t_{ren} = 10^{-3}$s	7.75×10^{-10}	1.24×10^{-8}
$t_{ren} = 10^{-5}$s	2.21×10^{-9}	1.80×10^{-8}
$t_{ren} = 10^{-6}$s	6.06×10^{-9}	3.21×10^{-8}
$t_{ren} = 10^{-7}$s	1.83×10^{-8}	7.18×10^{-8}
D_{2Dexp}	$9.6(\pm 2) \times 10^{-8}$	$2.5(\pm 0.08) \times 10^{-7}$

At the smallest renewal times, we compare the diffusion coefficient when the J_{ij} are drawn from the PACKMOL or the CPMD distributions. We can see opposite trend for the two dyes.

Table 6: Comparison of the diffusion coefficients calculated at fast renewal times with the distributions from CPMD and from PACKMOL

Case	D_{calc} / cm^2.s^{-1} with PACKMOL	D_{calc} / cm^2.s^{-1} with CPMD
D102 $t_{ren} = 10^{-6}$s	6.5×10^{-9}	6.03×10^{-8}
D102 $t_{ren} = 10^{-7}$s	3.3×10^{-8}	8.76×10^{-8}
D149 $t_{ren} = 10^{-6}$s	5.3×10^{-8}	3.21×10^{-8}
D149 $t_{ren} = 10^{-7}$s	9.2×10^{-8}	7.18×10^{-8}

For D102, the coefficients from the CPMD are higher than the ones from PACKMOL. This is because of the wide PACKMOL distributions for D102 which brings more weak J_{ij} than the CPMD distributions (Figure 4 b in the main text). On the other hand, the PACKMOL distributions for D149 are similar in shape to the CPMD distributions but with overall higher mean leading to higher diffusion coefficients.

This material is available free of charge via the Internet at `http://pubs.acs.org/`.

Graphical TOC Entry